

# Taming electronic decoherence in 1D chiral ballistic quantum conductors

C. Cabart<sup>1</sup>, B. Roussel<sup>1</sup>, G. Fève<sup>2</sup>, and P. Degiovanni<sup>1</sup>  
(1) *Univ Lyon, Ens de Lyon, Université Claude Bernard Lyon 1, CNRS, Laboratoire de Physique, F-69342 Lyon, France and*  
(2) *Laboratoire Pierre Aigrain, Ecole normale supérieure, PSL University, Sorbonne Université, Université Paris Diderot, Sorbonne Paris Cité, CNRS, 24 rue Lhomond, 75005 Paris France.*

Although interesting per se, decoherence and relaxation of single-electron excitations induced by strong effective screened Coulomb interactions in Quantum Hall edge channels are an important challenge for the applications of electron quantum optics in quantum information and quantum sensing. In this paper, we study intrinsic single-electron decoherence within an ideal single-electron channel with long-range effective Coulomb interactions to determine the influence of the material and sample properties. We find that weak-coupling materials characterized by a high velocity of hot-electron excitations may offer interesting perspectives for limiting intrinsic decoherence due to electron/electron interactions. We discuss quantitatively how extrinsic decoherence due to the coupling with the channel's electromagnetic environment can be efficiently inhibited in specially designed samples at  $\nu = 2$  with one closed edge channel and we propose a realistic geometry for testing decoherence control in an Hong Ou Mandel experiment.

PACS numbers: 73.23.-b, 73.43.-f, 71.10.Pm, 73.43.Lp

Keywords: quantum Hall effect, quantum transport, decoherence

## I. INTRODUCTION

Over the last decade, a considerable effort has been devoted to the development of quantum coherent nano-electronics with the aim of controlling electronic quantum transport down to the single particle level<sup>1,2</sup>. This has led to the development of electron quantum optics<sup>3</sup>, an emerging field which aims at manipulating electrons in a ballistic quantum conductor just as photons in quantum optical setups. This perspective had initially risen strong hopes for on-chip quantum information processing using single electrons as quantum information carriers<sup>4-6</sup>.

However, electron quantum optics differs from quantum optics because electrons, being charged, interact via effective screened Coulomb interactions. This leads to electronic decoherence and relaxation<sup>7</sup>. These effects are strong enough to destroy the electronic quasi-particle in the  $\nu = 2$  quantum Hall edge channel system, a fact first evidenced by non-equilibrium distribution relaxation studies<sup>8</sup> and later confirmed by recent studies of single-electron decoherence through Hong Ou Mandel (HOM) experiments<sup>9,10</sup>. Recent Mach-Zehnder interferometry (MZI) experiments<sup>11</sup> have also confirmed the plausibility of this scenario although the most commonly used model based on effective screened short-range interactions<sup>12</sup> fails to reproduce the observed saturation of the decoherence scenario<sup>13</sup>. These recent results suggest that our understanding of quantitative models of electronic decoherence still needs to be sharpened.

On the other hand, using single-electron excitation as carriers of quantum information requires a high degree of control from their generation to their detection, and of course during their propagation. Several single-electron sources have been developed over the years, from the mesoscopic capacitor<sup>14</sup> to single-electron pumps<sup>15,16</sup> and

more recently the Leviton source<sup>17</sup>. Other systems aim at injecting electrons at very high energies<sup>18</sup> using dynamically driven dots or at transporting them using surface acoustic waves<sup>19</sup>. The maturation of technology may lead to the development of controlled sources able to emit specifically tailored electronic wavepackets<sup>20-22</sup>.

On the detection side, a full quantum current analyzer has been developed to extract the single-electron wave functions present within a time-periodic electric current<sup>23</sup>. Dynamical quantum dots are envisioned to probe single-electron coherence in a time-dependent and energy-selective way<sup>16,24</sup>. But controlling the dynamics of propagating single to few electron excitations is still a challenge.

Understanding single to few electron decoherence is therefore crucial both for our understanding of electronic quantum transport and for the most promising applications of electron quantum optics such as quantum information processing and the quantum metrology of charge and electric currents. It is thus time to ask to what extent electronic decoherence can be tamed in experimentally relevant systems.

In this paper, we address this question within our recently developed non-perturbative framework for studying single-electron decoherence in a chiral 1D conductor<sup>25,26</sup>. More precisely, we will discuss the influence of the material properties (intrinsic and induced by its fabrication and gating) by considering single-electron decoherence induced by effective screened Coulomb interactions within an ideal dissipationless single chiral edge channel. Our study suggests that materials such as exfoliated graphene and AsGa respectively correspond to weak and strong coupling materials, the former being more favorable for preserving electronic decoherence than the latter. Beyond the specific example, we think that

this shows the importance of investigating electron quantum optics in various materials.

We then apply our approach to the question of passive decoherence control, that is through sample design. We present an in depth discussion of various geometries which have been used in recent experiments<sup>27,28</sup>. Our results suggest that an efficient control of single-electron decoherence could be achieved in realistic samples based on edge channels of an AsGa 2D electron gas in the integer quantum Hall regime at  $\nu = 2$ . A new sample design is proposed for testing our approach in a HOM interferometer. Let us stress that our work also points out to the possibility of discriminating among various models of effective screened electronic Coulomb interactions using HOM interferometry experiments. As a bonus, we will see that such devices offer interesting perspective for single edge magnetoplasmon generation, thus connecting electron quantum optics to quantum plasmonics and microwave quantum optics.

This paper is structured as follows: in Sec. II, we briefly review the basic concepts of electron quantum optics and the physics of single-electron decoherence in quantum Hall edge channels. Then, analytical models of screened Coulomb interactions for the physical situations relevant for the present paper will be introduced and the corresponding edge-magnetoplasmon scattering will be discussed. Section III is devoted to electronic decoherence. Decoherence at filling fraction  $\nu = 1$  in the dissipationless case will enable us to discuss the influence of the material. We will also discuss to what extent an HOM experiment could help discriminate between short and long-range effective interactions in the  $\nu = 2$  system. Finally, section IV is devoted to decoherence control for single-electron excitations by sample design.

## II. ELECTRON QUANTUM OPTICS AND FINITE-FREQUENCY QUANTUM TRANSPORT

### A. Electron quantum optics

The key concepts of electron quantum optics are electronic coherences defined by analogy with photon coherences introduced by Glauber for photons<sup>29</sup>. The first order electronic coherence at position  $x$ <sup>30-32</sup>  $\mathcal{G}_{\rho,x}^{(e)}(t|t') = \text{Tr}(\psi^\dagger(x,t)\rho\psi(x,t'))$ , where  $\psi$  is the electronic annihilation operator, contains all information on the single-electron wavefunctions that can be extracted from the system at position  $x$ . To simplify notation, because our detection setup is at a fixed position  $x$ , we will drop it from all equations in the following. Electronic coherence is most conveniently visualized using a real valued time/frequency representation called the electronic Wigner function, defined as<sup>33</sup>:

$$\mathcal{W}_\rho^{(e)}(t,\omega) = \int v_F \mathcal{G}_\rho^{(e)}\left(t + \frac{\tau}{2}, t - \frac{\tau}{2}\right) e^{i\omega\tau} d\tau \quad (1)$$

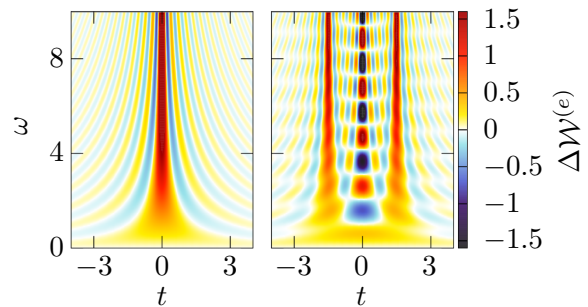


FIG. 1: (Color online) Left panel: excess electronic Wigner function for a single electronic state of the form  $\psi^\dagger(t=0)|F\rangle$  measured at  $x=0$ . Right panel: excess electronic Wigner function for a quantum superposition  $(\psi^\dagger(-\tau/2) + \psi^\dagger(\tau/2))|F\rangle/\sqrt{2}$  ( $\tau=3$  on this specific example). The interference contribution is clearly visible and overlaps with each localized excitation contribution for  $\omega\tau \lesssim 1$ .

The electronic Wigner function is directly related to physically relevant quantities: first of all, integrating over  $\omega$  leads to the average time-dependent current and time averaging gives the electronic distribution function. Moreover, the low-frequency Hong-Ou-Mandel noise signal for two electronic sources is directly proportional to the overlap of the excess Wigner functions of the two sources<sup>33</sup>, a fact directly exploited in electronic tomography protocols<sup>23,30,34</sup> and recent studies of electronic decoherence<sup>9,10</sup>.

Within the bosonization framework briefly reviewed in Appendix A, a single-electron excitation with wavepacket  $\varphi_e$  above the Fermi sea

$$|\varphi_e, F\rangle = \int_{-\infty}^{+\infty} \varphi_e(t)\psi^\dagger(t)|F\rangle dt \quad (2)$$

is a quantum superposition of coherent edge-magnetoplasmon states. The electronic Wigner function for a perfectly localized electronic excitation above the Fermi sea  $\psi^\dagger(0)|F\rangle$  is, up to normalisation, depicted on the left panel of Fig. 1. As expected from the Heisenberg uncertainty principle, such an excitation is not limited in energy and, when looked at energy  $\varepsilon > 0$  above the Fermi level, the Wigner function tends to spread over a time scale  $\hbar/\varepsilon$ . The Wigner function of a quantum superposition of two such excitations at times  $t_1$  and  $t_2$  contains a contribution for each of the excitations within the superposition and an interference contribution located at time  $(t_1 + t_2)/2$  as depicted on the right panel of Fig. 1.

When considering an arbitrary electronic wavepacket  $\varphi_e$ , these interference contributions are responsible for cancellations which, in the case of the Landau excitation emitted at energy  $\hbar\omega_0$  above the Fermi level, localize the main contribution to the excess electronic Wigner function close to  $\omega_0$ . This process is depicted on Fig. 2, in which the full excess electronic Wigner function is reconstructed from the excess Wigner function of a quantum

superposition of more and more localized electronic excitations at times  $t_j$ , each of them weighted by the value of the electronic wavefunction  $\varphi_e(t_j)$ . This specific Landau wavepacket, given by<sup>30,33</sup>

$$\tilde{\varphi}_e(\omega) = \frac{\mathcal{N}_0 \Theta(\omega)}{\omega - \omega_0 - i/2\tau_0} \quad (3)$$

where  $\tau_0$  denotes the excitation lifetime, will be used as our main example through this whole text because of its experimental relevance for the mesoscopic capacitor in the ideal single-electron source regime<sup>14,35,36</sup>. Note that the methods we have developed could also be used for making predictions for arbitrary injected single electron wavepackets and can therefore be combined with our recently developed quantum current analysis<sup>23,37</sup> which enables us to characterize possible single electron emission regimes from a Floquet modeling of the source and to extract the corresponding electronic wavefunction.

The other important example we use in this article is the recently observed<sup>38</sup> Leviton excitation introduced by Levitov, Lee and Lesovik<sup>39</sup> and whose wavepacket is given by

$$\varphi_e(t) = \sqrt{\frac{\tau_0}{2\pi}} \frac{1}{t + i\tau_0}. \quad (4)$$

This excitation is in fact quite different from other arbitrary wavepackets, as it is the only mono-electronic excitation that can be created by applying a carefully designed classical voltage drive to an ohmic contact<sup>40</sup>. Consequently, a Leviton is a coherent state of edge magnetoplasmons, an essential feature for understanding the effect of interactions on this state<sup>41</sup>. The Wigner functions for both types of single-electronic excitations used in this paper are depicted on Fig. 3.

## B. The physics of single-electron decoherence

In the original discussion of the decay of an electronic quasi-particle by Landau<sup>42</sup>, electronic decoherence arises from electron/hole pair creation by the time and space dependent electric potential generated by the bare charged injected at a given energy above the Fermi sea. More than 50 years later, the discovery of dynamical Coulomb blockade<sup>43,44</sup> showed us that electronic relaxation could also arise from the emission of photons within the electromagnetic environment of the conductor.

Our present understanding of single-electron decoherence in quantum Hall edge channels<sup>25,45</sup> appears as a combination of these two effects: (1) the many-body decoherence of the electronic fluid that arises from the capacitive coupling to external degrees of freedom such as the second edge channel in the  $\nu = 2$  system or charge modes of a neighbouring circuit and (2) the generation of electron/hole pairs in the same channel, induced by voltage fluctuations within the interacting region. These fluctuations are due to electron/electron screened Coulomb

interactions within the edge channel as well as from the backaction of Coulomb induced charge fluctuations from neighboring conductors.

Many-body decoherence arises from the entanglement between the charge degrees of freedom of the edge channel under consideration and external degrees of freedom. For example, at  $\nu = 2$ , Coulomb interactions induce entanglement between the two edge channels. It is responsible for the fast relaxation of Landau electronic excitations compared to the Levitov excitations<sup>45</sup>. This striking difference between these two excitations can be traced back to the fact that, Levitov excitations being edge-magnetoplasmon coherent states, they are pointer states<sup>46</sup> with respect to Coulomb interaction induced decoherence. On the other hand, all other single-electron excitation being quantum superpositions of such edge-magnetoplasmon coherent states, many-body decoherence kills interferences between these coherent components. This leads to a suppression of interferences between them at the single-electron level, thus causing its rapid relaxation in energy. As demonstrated by experimental decoherence studies at  $\nu = 2$  through HOM interferometry<sup>9</sup> as well as by Mach-Zehnder interferometry<sup>11</sup>, this is the dominant cause of electronic decoherence in these experiments so far.

On the contrary, when the edge channel is not coupled to external dynamical degrees of freedom, many-body decoherence is not present and single-electron decoherence only arises from the creation of electron/hole pairs within the electronic fluid. This purely intrinsic process can be interpreted as the spreading of electronic coherence associated with the injected single electron into higher order correlations. We expect it to be less stringent than excitation emission into the external environment due to Pauli principle induced phase space limitations. The decoherence scenario is thus expected to be significantly different and more favorable to decoherence control than when the edge channel is capacitively coupled to other conductors.

Inspired by this idea, we will therefore study electronic decoherence within an ideal  $\nu = 1$  quantum Hall edge channel. It is solely influenced by the intrinsic properties of the edge channel, that is the intrinsic and substrate material properties as well as its gating, thus giving us new insight on the first question motivating the present work.

Cutting off the possibility to generate excitations within the electromagnetic environment is also the basic idea behind passive decoherence protection by sample design at  $\nu = 2$ . The samples studied in Refs.<sup>27,28</sup> are based on blocking electronic relaxation and decoherence within one of the two edge channels by closing the other one on itself.

As known from previous studies<sup>25,26</sup>, quantitatively studying the electronic decoherence scenarios in these different situations requires an understanding of the effect of effective screened Coulomb interactions on the electronic fluid. As we shall recall now, in the linear response

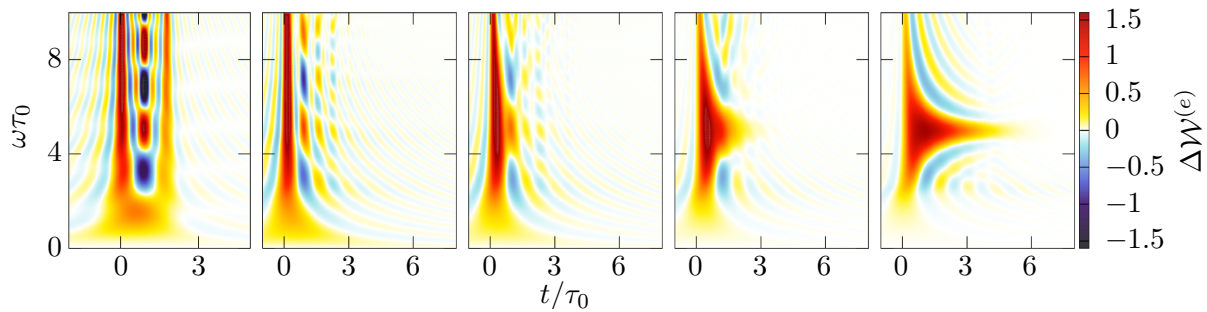


FIG. 2: Reconstruction of the excess Wigner function for a Landau excitation with emission energy  $\hbar\omega_0$  and duration  $\tau_0$  with  $\omega_0\tau_0 = 5$ . Each panel depicts the Wigner function associated with a finite sum  $\sum_{j=1}^N \varphi_e(t_j)\psi^\dagger(t_j)|F\rangle$  where the times  $t_j$  are sampled randomly using the probability distribution  $|\varphi_e(t)|^2$ . From left to right, panels show the results corresponding to  $N = 2, N = 10, N = 25, N = 100$  and  $N = 500$ . The specific form of any wavepacket can thus be seen as arising from the interference pattern between its different time-localized contributions.

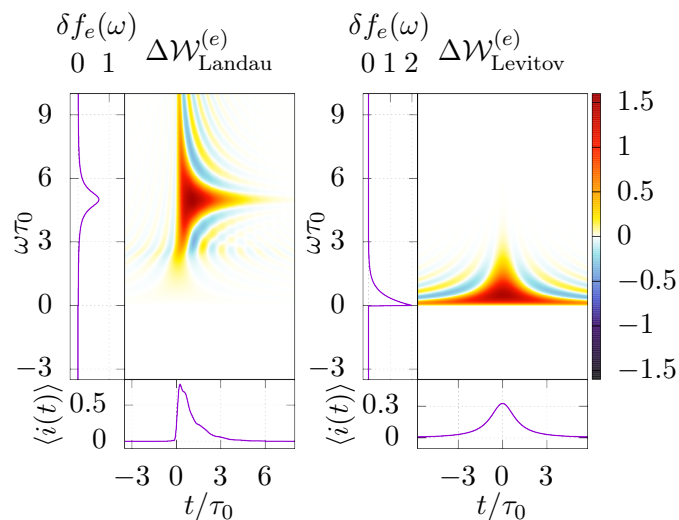


FIG. 3: (Color online) Density plot of the Wigner function of a Landau excitation with parameters  $\omega_0\tau_0 = 5$ , left, and an  $n = 1$  Leviton excitation, right, as a function of  $t/\tau_0$  and  $\omega\tau_0$ . Marginals are also plotted, giving access to the average current as a function of time (bottom of each plot) and the excess occupation number as a function of energy (left of each plot). These two excitations are single-electronic and are respectively energy- and time-resolved, with a Lorentzian profile. In the case of the Landau excitation, we recover the form given by the superposition depicted on Fig. 2.

regime, it is completely encoded into the finite-frequency admittance matrix of the system.

### C. Interactions and edge-magnetoplasmon scattering

#### 1. General method

During their propagation, electronic excitations experience screened Coulomb interactions within the conduc-

tor and with charges located in nearby conductors. However, in a regime of linear response for all conductors involved, interaction effects can be described within the edge-magnetoplasmon scattering formalism, which describes how the bosonic edge-magnetoplasmon modes are altered within the interaction region. This is why the bosonization framework provides the key for describing electronic coherence propagation along chiral edge channels.

More precisely, we consider a length  $l$  region of a quantum Hall edge channel in which electrons experience intra-channel Coulomb interactions as well as Coulomb interactions with other edge channels (see Fig. 4-(a)) or with an external gate connected to an impedance (see Fig. 4-(b)). For the edge channel under consideration, electronic degrees of freedom are described by the bosonic field  $\phi(x, t)$  defined from the charge density by (A1). Its equation of motion is given by

$$(\partial_t + v_F \partial_x)\phi(x, t) = \frac{e\sqrt{\pi}}{h} U(x, t) \quad (5)$$

where  $U(x, t)$  denotes the potential along the edge channel. Assuming we are in a linear screening regime within the edge channel as well as for the external elements capacitively coupled to it, the potential  $U(x, t)$  is linear in terms of both the bosonic fields associated with the other edge channels and bosonic dynamical variables describing other circuit elements. In the case of a gate coupled to an external circuit, these would be the bosonic modes associated with the transmission line representation of the circuit's impedance. In the same way, the edge-magnetoplasmon modes of the current channel appear within source terms for the linear equations that describe bosonic modes for the other edge channels and circuit elements.

The interaction region being of finite length, solving the full set of equations of motion leads to an expression for the outgoing fields in terms of the incoming fields. Note that because the problem is time translation invariant, the solution can be expressed in terms of an elastic scattering matrix  $S(\omega)$  linking the incoming and outgoing

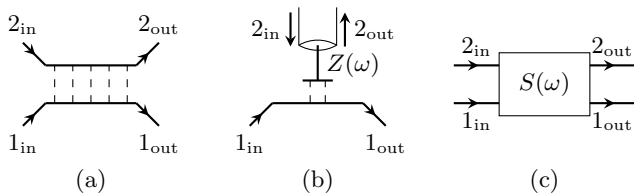


FIG. 4: (Color online) The edge-magnetoplasmon scattering approach describes many situations, such as for example (a) two copropagating edge channels capacitively coupled over a distance  $l$ , (b) a chiral edge channel capacitively coupled to a linear external circuit described by a frequency dependent impedance  $Z(\omega)$ . (c) Solving for the equation of motions leads to a frequency dependent scattering matrix  $S(\omega)$  between the channel's edge-magnetoplasmon modes and the bosonic modes of the other system.

bosonic modes (see Fig. 4 (c)). In the present situation where all the incoming and outgoing channels, outside of the interaction region, correspond to non-interacting edge channels with the same Fermi velocity, energy is conserved. In terms of edge-magnetoplasmon scattering, this implies that the scattering matrix is unitary. *diré*.

The edge-magnetoplasmon scattering matrix is directly related to the dimensionless finite-frequency admittance  $g_{\alpha,\beta}(\omega) = R_K G_{\alpha,\beta}(\omega)$  ( $R_K = h/e^2$  being the quantum of resistance) defined as the ratio of the derivative of total current coming into the sample through the edge channel  $\alpha$  with respect to the voltage applied to the reservoir feeding the edge channel  $\beta$ . Such a relation had been derived in the case of quantum wires<sup>47–49</sup> which are non-chiral Luttinger liquids. In the present case of chiral quantum Hall edge channel at integer filling fractions, it takes the following form<sup>50</sup>:

$$g_{\alpha\beta}(\omega) = \delta_{\alpha,\beta} - S_{\alpha\beta}(\omega). \quad (6)$$

Relating edge-magnetoplasmon scattering to response functions also puts some constraints on scattering amplitudes.

First of all, the dimensionless finite-frequency admittance  $g(\omega) = 1 - S_{11}(\omega)$  of the effective dipole formed by the interaction region of the edge channel 1 (lower part of Figs. 4-(a-c)) and all grounded elements it is capacitively coupled to (upper part of Figs. 4-(a-c)) is defined as:

$$g(\omega) = \left. \frac{\partial \langle \tilde{I}_1(\omega) \rangle}{\partial \tilde{V}_1(\omega)} \right|_{V_1=0} \quad (7)$$

where  $\tilde{I}_1(\omega)$  denotes the Fourier transform of the total current  $(i_{1,\text{in}} - i_{1,\text{out}})(t)$  and  $V_1(t)$  denotes the time dependent drive applied to the edge channel 1 keeping the rest at zero potential. Being a physical response function, its analytic continuation to negative frequencies obeys the reality condition:  $g(\omega)^* = g(-\omega)$ . Consequently,  $t(\omega) = S_{11}(\omega)$  can be analytically extended to negative frequencies by  $t(-\omega) = t(\omega)^*$ .

Next, the finite-frequency admittance  $g(\omega)$  is the one of a passive circuit. As such, it obeys the general property first proposed by Cauer<sup>51</sup> and then proven by Brune<sup>52</sup> of being positive real. With our convention, this means that for  $z = \sigma + i\omega$ ,  $z \mapsto g(z)$  is analytic in the half plane  $\Re(z) < 0$  and

$$\Re(g(z)) > 0 \quad \text{when } \sigma < 0 \quad (8a)$$

$$\Im(g(z)) = 0 \quad \text{when } z \in \mathbb{R}^- \quad (8b)$$

The analyticity condition ensures that the current response is causal and the two other conditions express that, when driven by a time-dependent voltage, the corresponding effective dipole dissipates energy and does not produce it. As we shall discuss, these conditions put some constraints on the low-frequency expansion of  $t(\omega)$  and consequently on the effective interaction models that can be used.

Finally, since the edge-magnetoplasmon scattering matrix depends on the precise form of the electric potential within the wire  $U(x, t)$ , analytical models are often approximative descriptions of the real physics of the sample. However, Eq. (6) suggests that edge-magnetoplasmon scattering amplitudes can be measured using finite-frequency admittance measurements. This has indeed been done in the case of the  $\nu = 2$  Quantum Hall edge channel system<sup>53</sup>.

As will be discussed in Sec. III, the edge-magnetoplasmon scattering amplitudes are the key ingredients for computing electronic decoherence<sup>45</sup>. Before turning to this problem, let us discuss several edge channel models starting with the case of an ideal  $\nu = 1$  edge channel with finite range intra-channel interactions. We shall then consider the case of two interacting edge channels ( $\nu = 2$ ) and discuss the case of specific geometries in which one of the edge channels is closed.

## 2. The $\nu = 1$ case

For a single edge channel with Coulomb intra-channel interactions, the edge-magnetoplasmon scattering matrix reduces to a frequency dependent transmission coefficient  $t(\omega)$  which, in the absence of dissipation, satisfies  $|t(\omega)| = 1$ .

Short-range effective screened Coulomb interactions correspond to a renormalization of the edge-magnetoplasmon velocity and therefore to a linear dependence of the phase of  $t(\omega)$  in  $\omega$ ,  $t(\omega) = e^{i\omega\tau(l)}$  where  $\tau(l)$  is the renormalized time of flight. By contrast, finite range interactions lead to a non-linear frequency dependence of the phase of  $t(\omega)$ . We shall write  $t(\omega) = e^{i\omega\tau(l,\omega)}$  where the time of flight now depends on  $\omega$  through a frequency dependent velocity for the edge magnetoplasmons,  $\tau(l,\omega) = l/v(\omega)$ . Since  $t(\omega)^* = t(-\omega)$ ,  $v(\omega)$  can be extended analytically to negative frequencies by  $v(-\omega) = v(\omega)$ .

A simple model of a  $\nu = 1$  edge channel with an interaction region of length  $l$ , capacitance  $C$  and bare

Fermi velocity  $v_F$  is presented in Appendix B. This model depends on a dimensionless coupling constant  $\alpha = (e^2/C)/(\hbar v_F/l)$  representing the ratio of the Coulomb energy for the interaction region to the associated kinetic energy. As expected, the edge-magnetoplasmon transmission amplitude  $t(\omega) = e^{i\omega l/v(\omega)}$  exhibits a non-linear dependence of the phase:

$$t(\omega) = e^{i\omega l/v_F} \frac{1 + A(\omega, l)e^{-i\omega l/(2v_F)}}{1 + A(\omega, l)e^{i\omega l/(2v_F)}} \quad (9)$$

where

$$A(\omega, l) = 4\alpha \operatorname{sinc}\left(\frac{\omega l}{2v_F}\right). \quad (10)$$

The edge-magnetoplasmon velocity  $v(\omega)$  decreases from  $v_0 = (1+4\alpha)v_F$  to its asymptotic value  $v_\infty = v_F$  showing some mild oscillations (see Fig. 5) arising from the sharp position dependence of the interaction potential at the boundary of the interaction region.

Realistic estimates for the coupling constant  $\alpha$  are given in Appendix B. In AsGa,  $\alpha \simeq 0.75$  for  $v_F \simeq 10^5$  m/s thus leading to a ratio  $v_0/v_F = 4$ . By comparison, a similar estimate for exfoliated graphene on a silicon oxide surface<sup>54</sup> leads to  $\alpha \simeq 0.05$  assuming  $v_F \simeq 10^6$  m/s, and thus to  $v_0/v_F \simeq 1.2$ . Provided it has such a high Fermi velocity, this specific form of graphene may thus correspond to a weak coupling whereas AsGa leads to strong coupling. A small coupling constant has drastic consequences on electronic decoherence as will be discussed in Sec. III C. Therefore, studying single-electron decoherence in the edge channels of graphene at  $\nu = 1$  may be a way to test whether or not it is a weak or a strong coupling material.

We expect a more realistic model of intra-channel interactions to lead to a qualitatively similar but smoother behavior of  $v(\omega)$ . Key features are the two different asymptotic velocities  $v_0$  and  $v_\infty$  in the limits  $\omega \rightarrow 0$  and  $\omega \rightarrow +\infty$ . The infrared velocity  $v_0$  is the velocity of low energy edge-magnetoplasmon modes and should therefore be called the plasmon velocity. Due to Coulomb interactions, it is expected to be higher than the velocity of high-energy excitations which do not experience interactions for a long time. Reasonable phenomenological models for  $v(\omega)$  should thus interpolate between  $v_0$  and  $v_\infty$  with  $v_0 > v_\infty$ . However, as explained in appendix E, the relation between  $t(\omega)$  and the finite-frequency admittance combined to Eqs. (8) strongly constrains the general form of the  $t(\omega)$ . It indeed rules out simple phenomenological expressions for the edge-magnetoplasmon velocity  $v(\omega)$ . Therefore, we shall discuss the ideal  $\nu = 1$  case using the long-range model presented in Appendix B.

### 3. The $\nu = 2$ case

The  $\nu = 2$  edge channel system is the simplest and experimentally most relevant case involving more than one

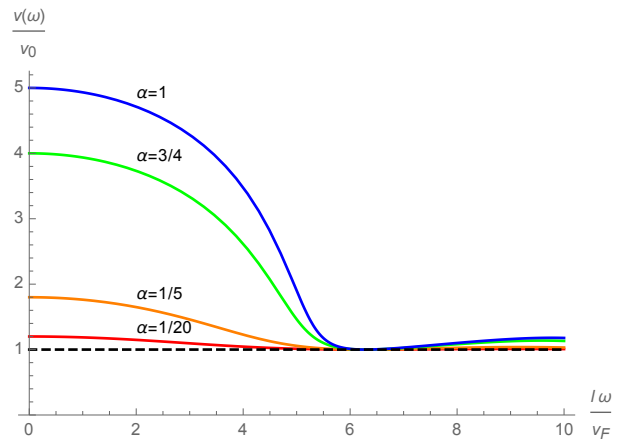


FIG. 5: (Color online) Velocity  $v(\omega)/v_0$  corresponding to  $\exp(i\omega l/v(\omega))$  given by Eq. (9) in terms of  $\omega l/v_F$  for  $\alpha = 1/20$  (graphene),  $\alpha = 1/5$ ,  $\alpha = 3/4$  (AsGa) and  $\alpha = 1$ .

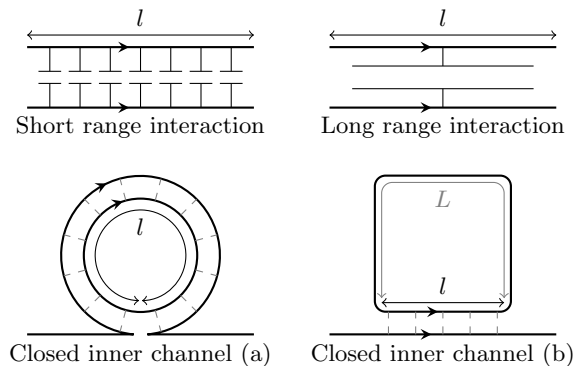


FIG. 6: Schematic view of the main types of interaction discussed at  $\nu = 2$ . Short-range interaction corresponds to a capacitive coupling between charge densities at the same position in the two channels, and no coupling between different positions. Long range interaction describes a situation where the system behaves as one big capacitor. We are also interested in situations where the inner channel is closed on itself and interacts with the outer channel either along its whole length (a), or only on a small portion of the closed loop (b). In either of these cases, interactions can be short range or long range.

channel. In this case, two copropagating edge channels separated by approximately 100 nm experience strong intra and inter-channel screened Coulomb interactions. Several models have been developed to describe this situation and are briefly reviewed here.

*a. Co-propagating channels with short-range interaction* In the presence of metallic side gates, Coulomb interactions are screened and the charge density in one channel is capacitively coupled to the charge density at the same point in the other channel<sup>12</sup>. More precisely, charge density in channel  $i$  at position  $x$  and energy  $\omega$   $\rho_i(x, \omega)$  is coupled to the local electrostatic potential  $U$  through distributed capacitances:  $\rho_i(x, \omega) = \mathcal{C}_{ij}U_j(x, \omega)$ . This model, schematically depicted on Fig. 6, is known

to give a good description of interactions in experimental systems at small energies, a fact that has been directly probed in the frequency<sup>53</sup> and time<sup>55</sup> domains and indirectly confirmed in Ref.<sup>56</sup>. Within the interaction region, edge-magnetoplasmon eigenmodes are delocalized over the two channels and propagate at different velocities. This leads to the following edge-magnetoplasmon scattering matrix<sup>50</sup>:

$$S(\omega) = \begin{pmatrix} p_+ e^{i\omega\tau_+} + p_- e^{i\omega\tau_-} & q (e^{i\omega\tau_-} - e^{i\omega\tau_+}) \\ q (e^{i\omega\tau_-} - e^{i\omega\tau_+}) & p_+ e^{i\omega\tau_-} + p_- e^{i\omega\tau_+} \end{pmatrix} \quad (11)$$

where

$$p_{\pm} = \frac{1 \pm \cos(\theta)}{2}, \quad q = \frac{\sin(\theta)}{2} \quad (12a)$$

$$\tau_+ = \frac{l}{v_+}, \quad \tau_- = \frac{l}{v_-}. \quad (12b)$$

In these equations,  $\theta$  corresponds to the coupling strength,  $v_+$  to the velocity of the slowest mode and  $v_-$  to the one of the fastest mode. In the strong-coupling regime,  $\theta = \pi/2$ , the corresponding modes are a fast charge mode, which is symmetric across both channels and an antisymmetric slow neutral mode<sup>12</sup>.

*b. Co-propagating channels with long-range interaction* The second model for interacting co-propagating channels assume that local potentials  $U$  are uniform on the whole length of the interaction region. The interaction region is a capacitor (see Fig. 6) and can be discussed in the spirit of the discrete element circuit models introduced by Büttiker *et al* for quantum conductors and quantum Hall edge channels<sup>57,58</sup>. This approach leads to the following edge-magnetoplasmon scattering matrix<sup>41</sup>:

$$S(\omega) = \begin{pmatrix} p_+ \mathcal{T}_+(\omega) + p_- \mathcal{T}_-(\omega) & q (\mathcal{T}_-(\omega) - \mathcal{T}_+(\omega)) \\ q (\mathcal{T}_-(\omega) - \mathcal{T}_+(\omega)) & p_+ \mathcal{T}_-(\omega) + p_- \mathcal{T}_+(\omega) \end{pmatrix} \quad (13)$$

where  $p_{\pm}$  and  $q$  are given by Eq. (12) and other parameters are given in terms of the dimensionless parameter  $x = \omega l / v_F$  by

$$\mathcal{T}_{\pm}(\omega) = \frac{e^{ix} - 1 + i\alpha_{\pm} x e^{ix}}{e^{ix} - 1 + i\alpha_{\pm} x} \quad (14)$$

$\alpha_{\pm}$  being linked to the eigenvalues of the capacitance matrix  $C_{\pm}$  by  $\alpha_{\pm} = R_K C_{\pm} v_F / l$ .

#### 4. The $\nu = 2$ case with a loop

Fig. 6(a) also depicts another situation that can be built with two copropagating edge channels, where the inner one is closed on itself over the length  $l$  where interaction takes place<sup>27</sup>. In the geometry depicted on Fig. 6(b), the same idea of a closed inner channel is used, but the copropagating distance over which interaction takes place is only a part of the total length of the loop. Such a geometry has been used for mitigating decoherence in electronic Mach-Zehnder interferometers<sup>28</sup>. Both

geometries impose a periodicity condition on the field for the inner channel:

$$\phi_2(0, \omega) = \phi_2(l, \omega) e^{i\omega\tau_L} \quad (15)$$

where  $\tau_L = \frac{L}{v_+}$  is the time it takes for an excitation to cover the non-interacting length  $L$  of the loop. The transmission coefficient is then obtained in full generality as

$$t(\omega) = S_{11}(\omega) + \frac{S_{12}(\omega) S_{21}(\omega)}{e^{-i\omega\tau_L} - S_{22}(\omega)}. \quad (16)$$

As expected, in the absence of dissipation, we have a unitary  $S$  matrix and this transmission coefficient has a modulus of 1. For short-range interaction, last equation specializes to

$$t(\omega) = -e^{i\omega(\tau_+ + \tau_- - \tau_L)} \left( \frac{e^{i\omega\tau_L} - p_+ e^{-i\omega\tau_+} - p_- e^{-i\omega\tau_-}}{e^{-i\omega\tau_L} - p_+ e^{i\omega\tau_+} - p_- e^{i\omega\tau_-}} \right) \quad (17)$$

Of course, the special case (a) is recovered for  $\tau_L = 0$ .

### III. ELECTRONIC DECOHERENCE

Let us now explain how to obtain the outgoing electronic coherences when a single-electron excitation is injected into the interaction region. We will first review the main steps and the essential points of the general methods developed for comparing the electronic decoherence of Landau and Levitov quasi-particles<sup>45</sup>. Then, we will discuss in details decoherence within a dissipationless single edge channel and then in the  $\nu = 2$  edge channel system.

#### A. General results

In the bosonization framework, the interaction region is a frequency dependent beam splitter for the edge-magnetoplasmon modes. An incoming coherent state for these modes is scattered exactly as a classical electromagnetic wave on an optical beam splitter<sup>41</sup>. More precisely, an incoming coherent edge magnetoplasmon of the form  $|\Lambda_1\rangle \otimes |\Lambda_2\rangle$  is transformed into an outgoing state  $|\Lambda'_1\rangle \otimes |\Lambda'_2\rangle$  where for all  $\omega > 0$ ,  $\Lambda'_\alpha(\omega) = \sum_{\beta} S_{\alpha\beta}(\omega) \Lambda_{\beta}(\omega)$ . Because single-electron states are described as quantum superposition of coherent edge-magnetoplasmon states, an exact description of the outgoing state after the interaction region can be obtained. A single-electron state injected in edge channel 1 corresponds, with the notations given in appendix A, to

$$|\varphi_e, F\rangle_1 \otimes |F\rangle_2 = \int_{-\infty}^{+\infty} \varphi_e(t) \frac{U_1^\dagger}{\sqrt{2\pi a}} \bigotimes_{\omega>0} (|\Lambda_\omega(t)\rangle_1 \otimes |0_\omega\rangle_2) dt \quad (18)$$

and comes out of the interaction region as:

$$\int \varphi_e(t) \frac{U_1^\dagger}{\sqrt{2\pi a}} \bigotimes_{\omega>0} (|t(\omega)\Lambda_\omega(t)\rangle_1 \otimes |r(\omega)\Lambda_\omega(t)\rangle_2) dt. \quad (19)$$

In this equation, we adopt the convention used in the remaining of this text that  $S_{11}(\omega) = t(\omega)$  and  $S_{21}(\omega) = r(\omega)$ , other coefficients of  $S$  being irrelevant as no injection is made in channel 2. Tracing on the second edge channel degrees of freedom leads to the reduced outgoing many-body density operator for the injection edge channel<sup>25</sup>:

$$\rho_1 = \int \varphi_e(t) \varphi_e^*(t') \mathcal{D}_{\text{ext}}(t-t') \psi^\dagger(t) |g(t)\rangle \langle g(t')| \psi(t') dt dt' \quad (20)$$

where  $\mathcal{D}_{\text{ext}}(t-t')$  is the extrinsic decoherence coefficient corresponding to the overlap of imprints left in the environment by localized electrons injected at times  $t$  and  $t'$ . It is given by<sup>25</sup> :

$$\mathcal{D}_{\text{ext}}(\tau) = \exp\left(\int_0^{+\infty} |r(\omega)|^2 (e^{i\omega\tau} - 1) \frac{d\omega}{\omega}\right). \quad (21)$$

The coherent edge-magnetoplasmon state  $|g(t)\rangle$  in Eq. (20) corresponds to the cloud of electron/hole pairs generated by Coulomb interactions when a localized electron  $\psi^\dagger(t)|F\rangle$  goes through the interaction region:

$$|g(t)\rangle = \bigotimes_{\omega>0} |(1-t(\omega))\Lambda_\omega(t)\rangle. \quad (22)$$

In the same way, in the  $\nu = 2$  case, the reduced density operator for the inner edge channel can be obtained by tracing out over the outer edge channel. This leads to

$$\rho_2 = \int \varphi_e(t) \varphi_e(t') \mathcal{D}_{\text{inj}}(t-t') |\mathcal{E}_2(t)\rangle \langle \mathcal{E}_2(t')| dt dt'. \quad (23)$$

where

$$|\mathcal{E}_2(t)\rangle = \bigotimes_{\omega>0} |r(\omega)\Lambda_\omega(t)\rangle \quad (24)$$

and the decoherence coefficient

$$\mathcal{D}_{\text{inj}}(\tau) = \exp\left(\int_0^{+\infty} |t(\omega)|^2 (e^{i\omega\tau} - 1) \frac{d\omega}{\omega}\right) \quad (25)$$

is equal to the overlap of the outgoing states  $|\mathcal{E}_1(t)\rangle$  of the injection edge channel corresponding to two different injection times:

$$|\mathcal{E}_1(t)\rangle = \bigotimes_{\omega>0} |t(\omega)\Lambda_\omega(t)\rangle. \quad (26)$$

This many-body description then gives access to all electronic coherence functions after the interaction region.

## B. Computing single-electron coherences

Let us now turn to first order coherences in the outer and inner channels after interaction, denoted respectively by  $\mathcal{G}_{\text{out},1}^{(e)}(t|t')$  and  $\mathcal{G}_{\text{out},2}^{(e)}(t|t')$ .

### 1. Outer channel coherence

When computing  $\mathcal{G}_{\text{out},1}^{(e)}(t|t')$ , the final results appear as a sum of two terms. The first one corresponds to a modification of the Fermi sea which, under the right condition, can be seen as the contribution of electron-hole pairs generated by Coulomb interaction vacuum state (namely the Fermi sea). This one is called the *modified vacuum*. Under the same condition, the second contribution comes from the incoming excitation elastically scattered or after interaction induced relaxation. This one is called the *wavepacket* contribution. These two contributions can be written as<sup>26</sup>

$$\mathcal{G}_{\text{MV},1}^{(e)}(t|t') = \int \varphi_e(t_+) \varphi_e^*(t_-) \mathcal{D}(t, t', t_+, t_-) \langle \psi^\dagger(t') \psi(t) \rangle_F \langle \psi(t_-) \psi^\dagger(t_+) \rangle_F dt_+ dt_- \quad (27a)$$

$$\mathcal{G}_{\text{WP},1}^{(e)}(t|t') = \int \varphi_e(t_+) \varphi_e^*(t_-) \mathcal{D}(t, t', t_+, t_-) \langle \psi(t) \psi^\dagger(t_+) \rangle_F \langle \psi(t_-) \psi^\dagger(t') \rangle_F dt_+ dt_- \quad (27b)$$

where

$$\mathcal{D}(t, t', t_+, t_-) = \gamma_+(t_+ - t') \gamma_-(t_+ - t) \gamma_+^*(t_- - t) \gamma_-^*(t_- - t') \quad (28)$$

is the effective single particle decoherence coefficient which takes into account both the action of environmental degrees of freedom and of electron-hole pairs cloud created in the injection channel. It is determined by the two functions

$$\gamma_\pm(t) = \exp\left(\pm \int_0^\infty \frac{d\omega}{\omega} (1 - t(\omega)) (e^{i\omega t} - 1)\right) \quad (29)$$

Explicit expressions for the two contributions (27a) and (27b) are given in Ref.<sup>45</sup> (Supplementary Material) and form the starting point of the numerical evaluation of the outgoing electronic coherence in the frequency domain (see Sec. III B 3).

An important quantity is the elastic scattering amplitude  $\mathcal{Z}(\omega)$  for an incoming single-electron excitation at energy  $\hbar\omega > 0$  which determines the inelastic scattering probability  $\sigma_{\text{in}}(\omega) = 1 - |\mathcal{Z}(\omega)|^2$ . Its expression is given by

$$\mathcal{Z}(\omega) = 1 - \int_0^\omega B_-(\omega') d\omega' \quad (30)$$

where  $B_-$  is defined as the regular part of the Fourier transform of  $\gamma_-$  and therefore satisfies the integral equation

$$\omega B_-(\omega) = t(\omega) - 1 + \int_0^\omega B_-(\omega') (t(\omega - \omega') - 1) d\omega' \quad (31)$$



with initial condition  $B_-(0^+) = -t'(\omega = 0^+)$ .

### 2. Inner channel coherence

Using the reduced density matrix  $\rho_2$  for the inner channel, any coherence function we are interested in can be computed. The main result is strikingly simple:  $\mathcal{G}_{\text{out},2}^{(e)}(t|t')$  is of the same exact form as  $\mathcal{G}_{\text{MV},1}^{(e)}(t|t')$  if we replace the function  $t(\omega)$  in the decoherence coefficient with  $1+r(\omega)$ . The fact that there is no wavepacket term emphasizes that no electron has been injected into the inner channel: only a cloud of electron/hole pairs is created.

### 3. Numerical method

As shown in Ref.<sup>45</sup> (Supplementary Material), the numerical evaluation consists in evaluating multiple integrals of factors. The implementation is quite straightforward, even though the main difficulty comes from the number of nested integrals (four for each point of the electronic coherence). For this, we use a frequency representation of the coherence. We discretize the input coherence on a grid using two directions,  $\omega$  and  $\delta\omega$ .  $\omega$  is the conjugate of  $t-t'$  and thus encodes the frequency dependence in the Wigner function.  $\delta\omega$  is the conjugate of  $(t+t')/2$ , and thus gives access to time dependance in the Wigner function. When there are  $n$  points in the input coherence in each direction  $\omega$  and  $\delta\omega$ , a naive implementation would require an  $\mathcal{O}(n^6)$  computation time. However, by exploiting the structure of the expressions, we have been able to lower the total complexity to  $\mathcal{O}(m \times n^4)$  where  $n$  denotes the number of points in the direction  $\omega$  and  $m$  the number of points in the direction  $\delta\omega$ . This structure allows us to decouple the two directions and, as such, we can have a better numerical evaluation by lowering the discretization step in the direction  $\omega$ , without touching to the direction  $\delta\omega$ , as long as we have enough information about the time evolution of the Wigner function. With these refinements and using the OpenMP parallel framework, a post-interaction coherence is computed within five to ten minutes on a 64 cores computer.

Exactly as in our previous work<sup>45</sup> (Supplementary Material), discretization steps are chosen by looking at errors. The trace of the excess single-electron coherence is the total charge injected and should not change. If this already very sensitive indicator is not enough, we compute the average outgoing electric current from the outgoing excess single-electron coherence and compare it to its value obtained by applying edge-magnetoplasmon scattering to the incoming average current. All graphs presented in the following exhibit errors smaller than 5% for those tests.

## C. Decoherence at $\nu = 1$

Let us first discuss electronic decoherence by using a crude physical picture for a single edge channel in which we have a low-frequency ( $\omega \lesssim \omega_c$ ) edge-magnetoplasmon velocity  $v_0$  greater than the high frequency ( $\omega \gtrsim \omega_c$ ) velocity  $v_\infty$ . This is an oversimplification of the model presented in Sec. II C 2 but it presents the key feature of having distinct high and low energy edge-magnetoplasmon velocities.

Since for  $\omega \gtrsim \omega_c$ , edge magnetoplasmons travel at the velocity  $v_\infty$ , decoherence only arises from the effective edge-magnetoplasmon scattering phase  $\tilde{t}(\omega) = t(\omega)e^{-i\omega\tau_\infty}$  which is roughly 1 for  $\omega \gtrsim \omega_c$  and  $e^{-i\omega\Delta\tau}$  for  $\omega \lesssim \omega_c$ , where  $\Delta\tau = \tau_\infty - \tau_0$  denotes the difference of time of flights between high and low energy edge magnetoplasmons. As interactions have an effective bandwidth  $\sim \omega_c$ , creation of electron/hole pair excitations happens close to the Fermi level (within one to a few  $\omega_c$ ). Consequently, for electronic excitations injected at a much higher energy, the corresponding low energy edge-magnetoplasmon modes can be viewed as an effective distinct environment for the high-energy electronic excitations<sup>25</sup>.

At lower energies, electronic decoherence also arises from the  $\omega$ -dependence of the edge-magnetoplasmon velocities but, at low enough frequency, a perturbative approach in  $\omega R_K C_\mu$  can be used. As we shall see, this leads to an expression of the inelastic scattering probability in terms of the effective description of the interaction region as a discrete element circuit, going beyond the series addition of the electrochemical capacitance  $C_\mu$  and the relaxation resistance  $R_K/2$ .

In the following, we shall first explore these high and low energy limiting regimes of electronic decoherence and then discuss the full physical picture of electronic decoherence and relaxation within a single isolated edge channel.

### 1. High energy decoherence and relaxation

For a single-electron excitation injected at high energy, the contribution to electronic coherence  $\varphi_e(t) \varphi_e^*(t')$  picks up an effective decoherence coefficient<sup>25</sup>  $\mathcal{D}(t-t')$ :

$$\Delta\mathcal{G}_{\text{WP}}^{(e)}(t|t') \simeq \varphi_e(t) \varphi_e^*(t') \mathcal{D}(t-t') \quad (32)$$

which, at  $\nu = 1$ , is equal to the overlap  $\langle g(t')|g(t) \rangle$  of the electron/hole pair clouds generated by Coulomb interactions:

$$\mathcal{D}(\tau) = \exp\left(\int_0^{+\infty} |1 - \tilde{t}(\omega)|^2 (e^{i\omega\tau} - 1) \frac{d\omega}{\omega}\right). \quad (33)$$

This description is analogous to the one used in the weak-coupling description of dynamical Coulomb block-

ade across a tunnel junction<sup>59</sup>. The relaxation kernel

$$\tilde{\mathcal{D}}(\omega') = \int_{-\infty}^{+\infty} e^{-i\omega\tau} \mathcal{D}(\tau) d\tau. \quad (34)$$

can then be decomposed into an elastic and an inelastic part:  $\tilde{\mathcal{D}}(\omega') = 2\pi(Z_\infty\delta(\omega') + d(\omega'))$  where

$$Z_\infty = \exp\left(-\int_0^{+\infty} |1 - \tilde{t}(\omega)|^2 \frac{d\omega}{\omega}\right) \quad (35)$$

is nothing but the high-energy limit of the elastic scattering probability  $|\mathcal{Z}(\omega)|^2$ . The inelastic part  $d(\omega)$  describes electronic relaxation: it represents the probability that the electron has lost energy  $\omega$ . It is determined by the integral equation

$$\begin{aligned} \omega d(\omega) &= |1 - \tilde{t}(\omega)|^2 \\ &+ \int_0^\omega |1 - \tilde{t}(\omega')|^2 d(\omega - \omega') d\omega'. \end{aligned} \quad (36a)$$

which can readily be solved on a computer using the initial condition that  $d(\omega \rightarrow 0^+) \rightarrow \lim_{\omega \rightarrow 0^+} (|1 - \tilde{t}(\omega)|^2/\omega)$ . It can also be expressed as a formal series corresponding to the various processes involving the emission of an increasing number of pairs of electron/hole excitations, exactly the same structure than in the dynamical Coulomb blockade theory<sup>59</sup>. With these notations, the elastic part of the outgoing Wigner function is well separated from the inelastic part:

$$\Delta\mathcal{W}_{\text{WP}}^{(e)}(t, \omega) = Z_\infty \mathcal{W}_{\varphi_e}(t, \omega) \quad (37a)$$

$$+ \int_0^\omega d(\omega') \mathcal{W}_{\varphi_e}(t, \omega + \omega') d\omega' \quad (37b)$$

where  $\mathcal{W}_{\varphi_e}(t, \omega)$  denotes the Wigner function associated to the incoming wavepacket  $\varphi_e$ . The incoming electron loses energy through electron/hole pair creation within a few  $\hbar\omega_c$  of the Fermi sea. As shown in Appendix C, in the present regime, one can show that for high-energy electrons, the amount of energy dissipated through electron/hole pair creations is small compared to their injection energy, thus providing us with an a posteriori validation of our approach.

The low energy electron/hole pairs will then propagate along at the low energy edge-magnetoplasmon velocity. In a first approximation, the physical picture for the decoherence and relaxation of single-electron excitations injected at high energy thus involves the incoming electron and its relaxation tail (described by Eq. (37)) propagating at the high-energy velocity  $v_\infty$  and the corresponding low energy electron/hole pairs propagating at the low energy edge-magnetoplasmon velocity  $v_0$ . This simple picture justifies interpreting  $v_\infty$  as the velocity of hot electrons whereas  $v_0$  is viewed as a plasmon velocity.

## 2. Low energy decoherence and relaxation

At low frequency, the effective dipole associated with the interaction region does not respond to a dc bias and

can thus be described in terms of a frequency dependent admittance  $G(\omega)$  in series with a capacitor  $C_\mu$  (see Fig. 7). As explained in Appendix D, the corresponding transmission coefficient  $t(\omega) = 1 - g(\omega)$  has modulus one if and only if  $\Re(1/G(\omega)) = R_K/2$  meaning that the circuit involves the relaxation resistance  $R_g = R_K/2$  in series with a purely reactive impedance. The simplest model for this pure reactance consists of an  $LC$  circuit depicted on the left panel of Fig. 7. The  $RC$ -time  $\tau_0 = R_K C_\mu$  of the circuit corresponds to the time of flight of low energy edge magnetoplasmons across the interaction region. Deviations from this behavior will lead to single-electron decoherence.

At low energy, a perturbative approach detailed in Appendix F leads to its description in terms of the discrete element circuit parameters  $\tau_0$ ,  $L$  and  $C$ . The inelastic scattering probability across the interaction region is then given by

$$\sigma_{\text{in}}^{(\text{pert})}(\omega) = \frac{11\alpha_3^2}{180} (\omega\tau_0)^6 + \frac{5\alpha_3\alpha_5}{42} (\omega\tau_0)^8 + \mathcal{O}((\omega\tau_0)^9). \quad (38)$$

where the inductance  $L$  is directly related to the  $\alpha_3$  coefficient and the capacitance  $C$  only contributes to the next order:

$$\tau_0 = R_K C_\mu \quad (39a)$$

$$\alpha_3 = \frac{L/R_K}{R_K C_\mu} - \frac{1}{12} \quad (39b)$$

$$\alpha_5 = \frac{1}{80} - \frac{1}{4} \frac{L/R_K}{R_K C_\mu} + \left(\frac{L/R_K}{R_K C_\mu}\right)^2 \left(1 + \frac{C}{C_\mu}\right) \quad (39c)$$

This connects the inelastic scattering probability for an incoming electron to the low-frequency discrete element circuit description for the interaction region.

A complementary understanding can be obtained by relating the finite-frequency admittance to the edge magnetoplasmon's effective velocity  $v(\omega)$  within the interaction region using  $t(\omega) = \exp(i\omega l/v(\omega)) = 1 - g(\omega)$  (see Appendix F). The effective circuit of Fig. 7 corresponds to a low-frequency expansion of  $v(\omega)$  of the form:

$$\frac{v(\omega)}{v_0} = 1 + \left(\frac{1}{12} - \frac{L/R_K}{R_K C_\mu}\right) (R_K C_\mu \omega)^2 \quad (40a)$$

$$- \left[\frac{C}{C_\mu} \left(\frac{L/R_K}{R_K C_\mu}\right)^2 - \frac{1}{12} \frac{L/R_K}{R_K C_\mu} + \frac{1}{180}\right] (R_K C_\mu \omega)^4 \quad (40b)$$

$$+ \mathcal{O}((\omega R_K C_\mu)^6) \quad (40c)$$

where  $R_K C_\mu$  is the low-frequency time of flight  $l/v_0$ . This expansion directly connects the discrete circuit element parameters  $L$  and  $C$  to the low-frequency behavior of  $v(\omega)$ . The value  $L = C_\mu R_K^2/12$  corresponds to a frequency dependency  $v(\omega) = v_0 + \mathcal{O}((R_K C_\mu \omega)^4)$ . For  $0 \leq L < C_\mu R_K^2/12$ , the velocity of edge magnetoplasmons starts first to increase quadratically at low-frequency, whereas  $v(\omega)$  directly starts decreasing for

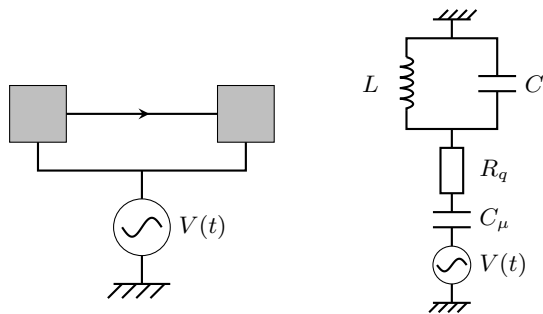


FIG. 7: (Color online) Left panel: effective dipole associated with the interaction region. Right panel: equivalent effective  $ZC$ -circuit at low-frequency. The resistive part of  $Z(\omega)$  is the relaxation resistance  $R_q = R_K/2$  and its imaginary part comes from an  $LC$  circuit.

$L > C_\mu R_K^2/12$ . Note that a higher inductance contributes to a stronger slow-down of the edge magnetoplasmons with increasing frequency, as expected for an inductive effect. The order 4 term given by Eq. (40b) describes the behavior of the plasmon velocity beyond this first order and contributes to its decrease with increasing frequency.

Coming back to the electronic inelastic scattering probability given by Eq. (38), the case where  $L = R_K^2 C_\mu/12$  minimizes its growth: the first non zero term is at order  $(\omega\tau_0)^{10}$ . This reflects the fact that for  $L = R_K^2 C_\mu/12$ , the distortion of a percussional current pulse is minimal at low-frequencies.

When  $\alpha_3 \neq 0$ , the first and second non trivial orders in  $\omega\tau_0$  compete as soon as  $\alpha_3\alpha_5 < 0$ , which means that they also compete in the expansion of the edge-magnetoplasmon time of flight as a function of frequency. This is the case when using the phenomenological form for the edge-magnetoplasmon velocity given by Eq. (E1).

### 3. Numerical results at $\nu = 1$

Let us now illustrate these discussions by using an  $\omega$ -dependent unit modulus transmission  $t(\omega)$  given by the long-range interaction model of Sec. II C 2. The corresponding  $R_K C_\mu$  time is  $l/v_0$  and expressions for the inductance  $L$  and capacitance  $C$  of the discrete element circuit are given by Eq. (D6). We will discuss both the case of a strong-coupling material ( $\alpha = 0.75$ ) and of a weak-coupling material ( $\alpha \simeq 0.05$ ).

Fig. 8 presents the elastic scattering probability  $|\mathcal{Z}(\omega)|^2$  as a function of  $\omega R_K C_\mu = \omega l/v_0$  for these two values of the coupling constant as well as for intermediate values  $\alpha = 1/10$  and  $\alpha = 1/4$ . At strong coupling, the low energy almost flat plateau close to unity is followed by a very strong decay of  $|\mathcal{Z}(\omega)|^2$  when  $\omega R_K C_\mu \gtrsim 2\pi$  towards a very small value. The low-coupling case also leads to a decay of the elastic scattering probability when  $\omega R_K C_\mu \gtrsim 2\pi$  but towards a higher value,  $Z_\infty \simeq 0.9$ .

Fig 9 depicts the asymptotic value  $Z_\infty$  of the elastic

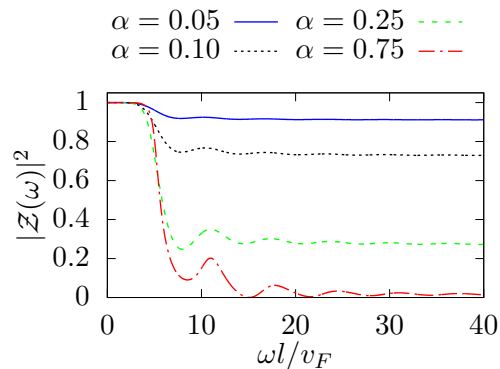


FIG. 8: (Color online) Elastic scattering probability for a single-electron excitation as a function of  $\omega l/v_F$  for the long-range interaction model given by Eq. (B5), for different values of the coupling constant  $\alpha$ .

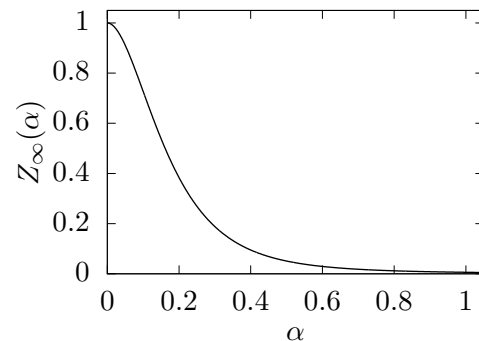


FIG. 9: (Color online) Asymptotic elastic scattering probability for high energy electrons  $Z_\infty(\alpha)$  given by Eq. (35) as a function of the coupling constant  $\alpha$  for the model introduced in Sec. II C 2. The inset shows the relaxation tail  $d(\omega)$  defined by Eq. (36) which gives the probability distribution for energy loss  $\hbar\omega$  by an incoming very high energy electron as a function of  $\omega l/v_F$  for the same values as Fig. 8, with the same color code.

scattering probability  $|\mathcal{Z}(\omega)|^2$  at high energy as a function of the coupling constant  $\alpha$  in the model of Sec. II C 2. Note that this is also the asymptotic elastic scattering probability for a finite energy single electron excitation in the limit  $l \gg v_0/\omega_0$ . We clearly see the difference between weak and strong coupling on electronic decoherence of high energy excitations: for  $\alpha = 0.05$ ,  $Z_\infty \simeq 0.91$  whereas for  $\alpha = 0.75$ ,  $Z_\infty \simeq 0.015$ .

Fig. 10 depicts the ratio of the full inelastic scattering probability to the perturbative expression as a function of  $\omega$ . It shows that the perturbative result is only valid at low energies, that is significantly before the drop of the elastic scattering probability, when the inelastic scattering probability is still very close to unity. Understanding the full behavior of the elastic scattering probability indeed requires a full non perturbative approach even at weak coupling because, at higher injection energies, mul-

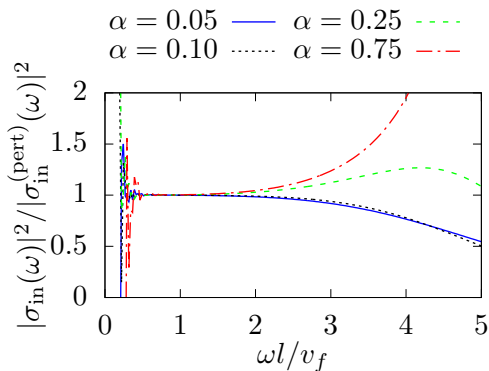


FIG. 10: (Color online) Ratio of inelastic scattering probabilities for the full model to its perturbative circuit expansion (38) at low energy. Numerical errors at small  $\omega l/v_F$  are due to the rapid decay of the dominant  $(\omega l/v_F)^6$  asymptotic behavior of the inelastic scattering probability at very low energies.

multiple low energy electron/hole pair emissions coexist with the emission of single electron/hole pair of higher energy. Properly accounting for all these processes requires the full knowledge of the frequency dependence of  $g(\omega)$  for which the simplest discrete element circuit descriptions are not sufficient.

Fig. 11 presents the electronic decoherence of an incoming wavepacket injected at energy  $\omega_0 R_K C_\mu = 15$ . In the weak-coupling case, we clearly see the separation in energy between the elastically scattered electronic excitation together with its relaxation tail at high energy and the resulting electron/hole pairs close to the Fermi level. This is expected since the elastic scattering probability is quite high at the injection energy. The temporal separation which is a result of the difference between the hot-electron velocity  $v_\infty$  and the plasmon velocity  $v_0$  is also clearly visible on the average electric current  $\langle i(t) \rangle$ : the sharp rise of the current corresponds to the arrival of the elastically scattered quasi-particle and  $t = 0$  corresponds to propagation at the fastest velocity  $v_0$ .

By contrast, in the strong-coupling case, electronic decoherence is much stronger. The relaxation tail of the incoming excitation is visible as a sharp rise of the current which arrives later than the beginning of the neutral electron/hole pair cloud. As expected the difference between the plasmon and high-energy electron velocities is also more important than in the weak-coupling case.

These results can be compared to the ones depicted on Fig. 12 which presents the electronic decoherence of an incoming wavepacket injected at  $\omega_0 R_K C_\mu \simeq 3$ , an energy lower than the previously discussed threshold. Most of its spectral weight is below the threshold. The Landau quasi particle propagates without experiencing much decoherence in both cases. We also see that it propagates at the low energy edge-magnetoplasmon velocity  $v_0$ . As expected, the incoming excitation seems less altered at weak coupling ( $\alpha = 0.05$ ) than at strong coupling ( $\alpha = 0.75$ ).

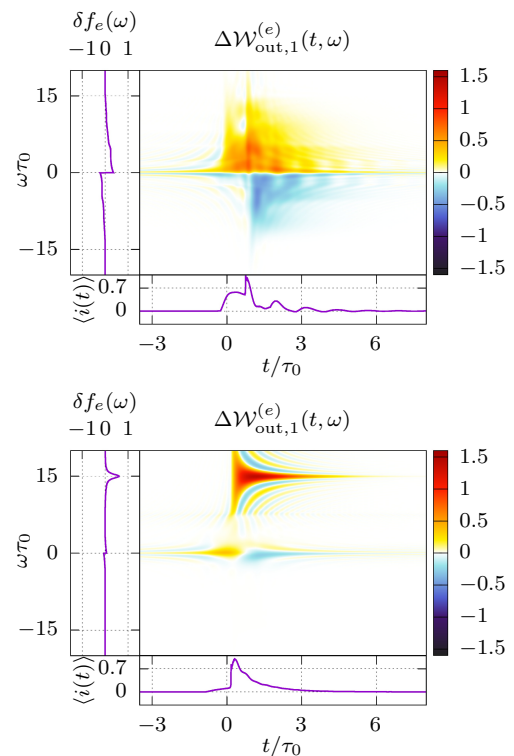


FIG. 11: (Color online) Wigner distribution function of an incoming wavepacket injected at energy  $\omega_0 R_K C_\mu = 15$ . Top panel: outgoing single-electron coherence for  $\alpha = 0.75$ . Bottom panel: outgoing single-electron coherence for  $\alpha = 0.05$ .  $t = 0$  corresponds to the expected time of reception for a free propagation at the low energy velocity  $v_0$ .

The main tool to test robustness to decoherence that can be used in electron quantum optics is an Hong Ou Mandel experiment<sup>60,61</sup>. It is then natural to think that strong and weak coupling regimes would lead to quantitatively different results in such experiments. In order to answer this question, we have computed the HOM signal, which is the excess HOM normalized noise obtained as the overlap of the incoming Wigner functions<sup>33</sup>, in both cases. Results are shown on Fig. 13 for both injection energies and both coupling values. As was discussed when looking at the Wigner functions, these curves confirm that weak coupling materials would lead to a stronger protection against decoherence.

#### 4. Commenting on AsGa vs graphene.

As discussed above, exfoliated graphene on a silicon oxide surface may correspond to a weak coupling value of  $\alpha$  and thus to much lower electronic decoherence. Moreover, provided velocities in graphene are much higher than in AsGa, the crossover energy between the low and high energy regimes should be much higher for fixed device dimensions. For example, a  $l = 20 \mu\text{m}$  propagation distance corresponds to  $\omega/2\pi = v_F/l \simeq 500 \text{ GHz}$  for

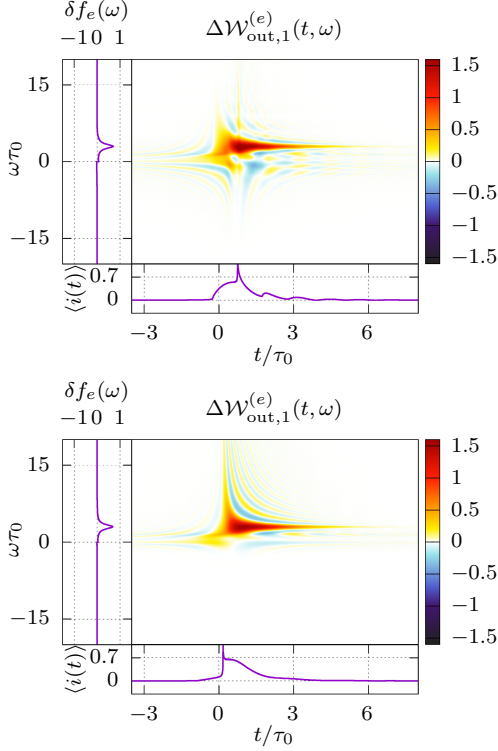


FIG. 12: (Color online) Wigner distribution function of an incoming wavepacket injected at energy  $\omega_e R_K C_\mu = 3$ . Top panel: outgoing single-electron coherence for  $\alpha = 0.75$ . Bottom panel: outgoing single-electron coherence for  $\alpha = 0.05$ .  $t = 0$  is the expected time of reception for a free propagation at the low energy velocity  $v_0$ .

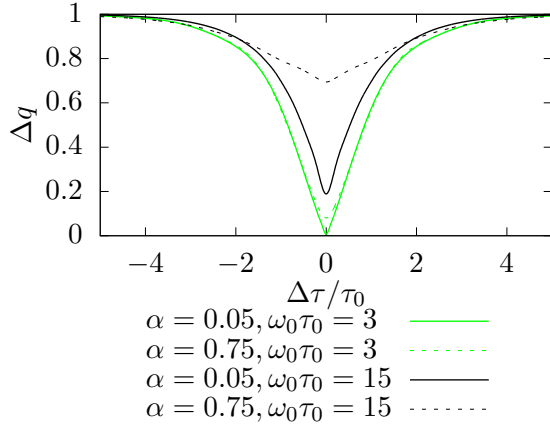


FIG. 13: (Color online) Theoretical results of an Hong-Ou-Mandel interferometry experiment obtained from the Wigner functions displayed in Figs. 11 and 12. As expected from the Wigner functions themselves, low energy excitations ( $\omega_0 \tau_0 = 3$ ) present a high contrast HOM dip. The results for high-energy excitations ( $\omega_0 \tau_0 = 15$ ) are clearly different between a weak coupling ( $\alpha = 0.05$ ) and a strong coupling ( $\alpha = 0.75$ ) material, thus providing a clear signature of the protection against decoherence offered by weak coupling materials.

$v_F = 10^6 \text{ m s}^{-1}$  and to 50 GHz for  $v_F = 10^5 \text{ m s}^{-1}$ .

The single-electron source based on the mesoscopic capacitor that has been developed in AsGa generates electronic excitations at an energy comparable to this crossover scale. With our estimated parameters, strong electronic decoherence is expected for a propagation above  $30 \mu\text{m}$  when injecting at an energy of the order of  $40 \mu\text{eV}$ <sup>75</sup>. Although no single-electron source has been developed yet for graphene in the quantum Hall regime, the ratio of estimated high-energy velocities in the two materials suggests a propagation distance of the order of  $200 \mu\text{m}$  in a  $\nu = 1$  ideal channel before any significant step in the inelastic scattering probability manifests itself in graphene. Moreover, as discussed in the previous section, even for such long propagation distances, electronic decoherence would be much lower in a weak coupling material compared to the case of a strong coupling material (see Fig. 9).

Of course, this discussion has been made within the framework of our model for electronic propagation within an ideal  $\nu = 1$  edge channel. In practice, it is known that edge magnetoplasmons propagating along quantum Hall edge channels experience dissipation<sup>53,54,62–64</sup>. This is one of the possible causes for missing energy in electronic relaxation experiments<sup>30</sup>. Investigating edge-magnetoplasmon dissipation effects on single-electron decoherence is certainly very important but this would go beyond the scope of the present paper. Nevertheless, we think that the main point stressed in the present paragraph, that is the effect of the Fermi velocity difference on the coupling constant and on the length to time scale conversion may lead to important differences between strong and weak-coupling materials concerning single-electron decoherence. As suggested by Fig. 13, HOM experiments may offer clear discriminating signatures of weak versus strong coupling materials but this would require the experimental development of single electron sources for Landau quasi-particles injection in graphene quantum Hall edge channels.

On the experimental side, a Mach-Zehnder interferometer has recently been demonstrated with encapsulated monolayer graphene sheet embedded within hexagonal boron nitride<sup>65</sup>. The beam splitters exploit same-spin intervalley scattering at a pn junction and the interferometer's geometry is controlled by Coulomb exchange interactions. Surprisingly, a contrast of 90 % has been observed at low bias in a parameter regime where one arm consists of one carrier edge channel and the other or two and for an arm length of  $1.2 \mu\text{m}$ . Such a high contrast remains up to a bias voltage larger than  $200 \mu\text{V}$ . Although decoherence mechanisms have not been yet studied in great detail for this device, we think that such a surprisingly high contrast as well as our discussion of coupling constant and high energy velocity effects call for intensive studies of single-electron decoherence in a material such as graphene.

## D. Decoherence at $\nu = 2$

Let us now turn to the  $\nu = 2$  case, which has already been studied in relation with experiments<sup>26,66</sup>. In the present case, we shall briefly recall the results obtained using the dispersionless model for edge-magnetoplasmon scattering between two strongly coupled copropagating edge channels (short-range interactions in Sec. II C 3) before discussing the influence of the finite range of interactions in an Hong-Ou-Mandel experiment.

### 1. Short-range interactions

Numerical results for both outer and inner channel coherences in the specific case of short-range interaction at strong coupling are presented on Fig. 14 for the Leviton source and on Fig. 15 for an energy-resolved excitation. Two distinct behaviours can be seen on these results. In the case of the Leviton source, the emitted state is a coherent state of plasmons created by the application of a classical voltage drive to an ohmic contact. Its evolution is dominated by fractionalization: we observe a simple separation of the incoming packet into two modes, one symmetric over the two channels and the other antisymmetric (see Fig. 14). In the outer channel, we recover exactly a fractionalization of the incoming excitation into two Levitons with charges  $-e/2$ , as was predicted in various theoretical works<sup>41,67</sup> and demonstrated experimentally<sup>10,53,68</sup>.

As recalled in Sec. II B, a Landau type excitation illustrates a different scenario: before fractionalization takes place, many-body decoherence leads to a fast energy relaxation with a strong decay of the weight around the injection energy, as can be seen on the upper panel of Fig. 15. This theoretical scenario and the corresponding quantitative predictions<sup>26,66</sup> have recently been confirmed by experiments<sup>9</sup>. The lower panel of Fig. 15 shows the electronic coherence in the inner channel. Although most excitations are created close to the Fermi level, we also see excitations created around the injection energy (for electrons) and close to the opposite (for the holes), which are the inner channel equivalent of the elastically scattered part still present in the outer channel.

### 2. Long-range interactions

At  $\nu = 2$ , a long-range interaction model can be studied (see Sec. II C 3) and may be experimentally relevant at higher energies<sup>53</sup>. The outgoing Wigner functions for excitations crossing a long-range interaction region are shown on Fig. 16. Several qualitative differences with the short-range case can be observed. First, we see non-vanishing coherence and current at negative times, the reference being given by the time taken for a free excitation to cross this interaction region. This is due to the long-range characteristics of interactions: as soon as the

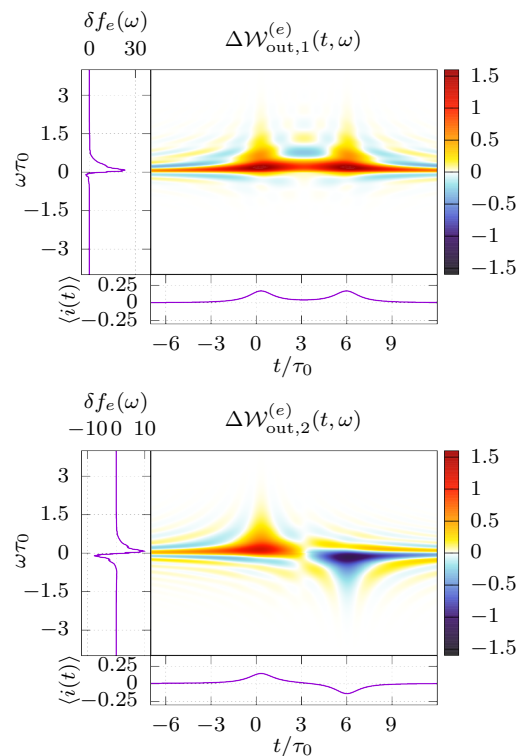


FIG. 14: (Color online) Wigner function for the outer (top) and inner (bottom) channel, for a Leviton excitation of width  $\tau_0$ . We use short-range interaction with parameters  $\theta = \pi/2$ ,  $\tau_+ = 6\tau_0$  and  $\tau_- = \tau_+/20$ . Since we inject a coherent state of plasmons, it fractionalizes into half-excitations and exhibits the behaviour of spin-charge separation, with the apparition of a fast symmetric mode over the two channels and a slow antisymmetric one.

incoming excitation enters the interaction region, it influences the whole interaction region and the contribution of the resulting low energy electron/hole pairs can be seen near its ends. This means that a first current peak should begin at a time  $\tau = l/v_F$  before the arrival of the “real” excitation as can be seen on the figure. Speaking of current, the bottom panel shows that the outgoing current has three main peaks, compared to the two obtained in a short-range setting.

It is then natural to ask whether or not these differences can be detected by an HOM experiment. To answer this question, the top panel of Fig. 17 displays our prediction for both the short and long-range interaction models assuming interaction regions of the same length and the same incoming excitations. As seen from this figure, these two interaction models lead to qualitatively different HOM curves: the long-range one shows a wider dip, as expected of the wider time spreading of the outgoing excitation and more “secondary dips” than the short-range model. This last feature can be traced back to the three main peaks in the outgoing Wigner function computed using the long-range model compared to the two peaks of short-range interactions.

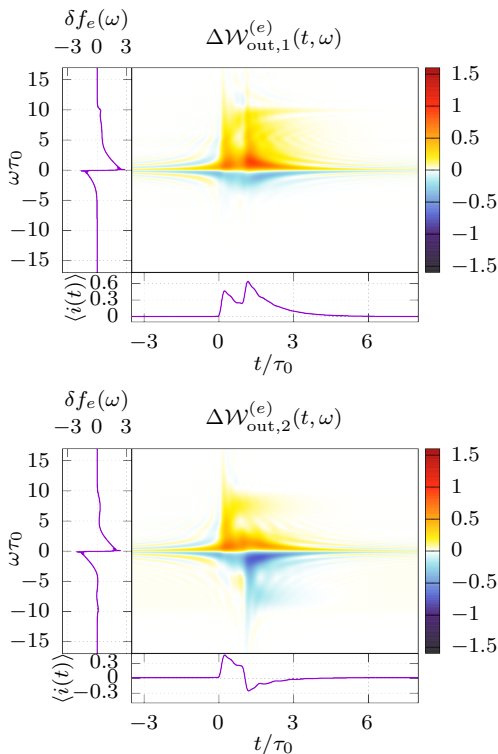


FIG. 15: (Color online) Wigner function for the outer (top) and inner (bottom) channel for a Landau excitation with parameters  $\omega_0\tau_0 = 10$ . Interaction parameters are  $\theta = \pi/2$ ,  $\tau_+ = \tau_0$  and  $\tau_- = \tau_+/20$ . In that case, the incoming state is a superposition of coherent plasmonic states. Interactions lead to the destruction of coherences between those states, and the end result is therefore a statistical mixture of coherent plasmonic states, whose energy content is no more resolved around  $\omega_0$ . In the time domain, since all bosonic states exhibit spin-charge separation when they pass through the interaction region, we recover once again this type of separation for the electric current.

To comment on the experimental state of the art<sup>9,10</sup>, we have plotted on the bottom panel of Fig. 17 the HOM predictions for parameters corresponding to the recently published experimental results in Ref.<sup>9</sup> Unfortunately the side lobes that would enable us to differentiate between the two interaction models occur for a time shift comparable or greater than 300 ps. However, probing time shifts larger than 200 ps brings us to values too close to the half-period of the drive which is typically 1 ns. In such situations, it is not possible anymore to forget about the excitation emitted in the other half period: we cannot rely on a single-electron decoherence computation for a quantitative theory/experiment comparison. Probing such large time shifts while comparing to our present theoretical predictions would therefore require lowering the drive frequency  $f$  thus deteriorating the signal to noise ratio of the low-frequency current noise measurements.

In our opinion, this calls for complementary investigations and/or experimental developments in order to determine which interaction model for the  $\nu = 2$  edge

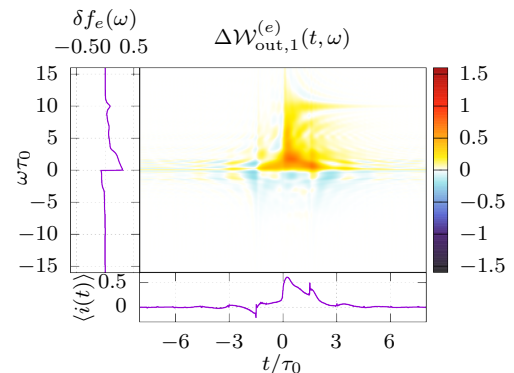


FIG. 16: (Color online) Wigner function of the outer channel for a Landau excitation with  $\omega_0\tau_0 = 10$  going out of a long-range interaction zone in the strong interaction regime ( $\theta = \pi/2$ ), with parameters  $l/v_F = 1.5\tau_0$ ,  $\alpha_+ = 1/2$  and  $\alpha_- = 1/59$ . The finite-frequency admittance of this interaction region has the same low energy limit than a short-range interaction region with parameters  $\tau_+ = \tau_0/2$ ,  $\tau_- = \tau_+/20$ . Differences between the long and short-range cases are the apparition of excitations at earlier times, three main peaks in the current instead of two, and a more complex pattern at low energies.

channel system would be the best at reproducing the full HOM curves in detail. By contrast, samples specifically designed for blocking relaxation processes are likely to give much stronger experimental signatures as will be discussed in the forthcoming section.

#### IV. DECOHERENCE CONTROL

In this section, we will consider passive decoherence control by sample design in the  $\nu = 2$  edge channel system. The idea is to combine the efficient screening of the edge channel used to propagate the injected electronic excitation to the blocking of energy transfers by closing the other edge channel. In a first experiment<sup>27</sup>, electronic relaxation in the outer edge channel has been partially blocked by letting the outer channel propagate along a closed inner edge channel as depicted on Fig. 6(a). In a more recent Mach-Zehnder interferometry experiment, electronic decoherence has been partially blocked by bordering the propagating edge channel by closed loops<sup>28</sup> as depicted on Fig. 6(b).

We shall now discuss electronic decoherence within both types of samples. We will first discuss what happens to Levitons by looking at edge-magnetoplasmon scattering in the time domain. Understanding this scattering in the frequency domain will then enable us to discuss electronic decoherence of a Landau excitation injected at various energies in Sec. IV B. Finally, a realistic possible sample design for probing the blocking of single-electron decoherence with HOM interferometry will be discussed in Sec. IV C.

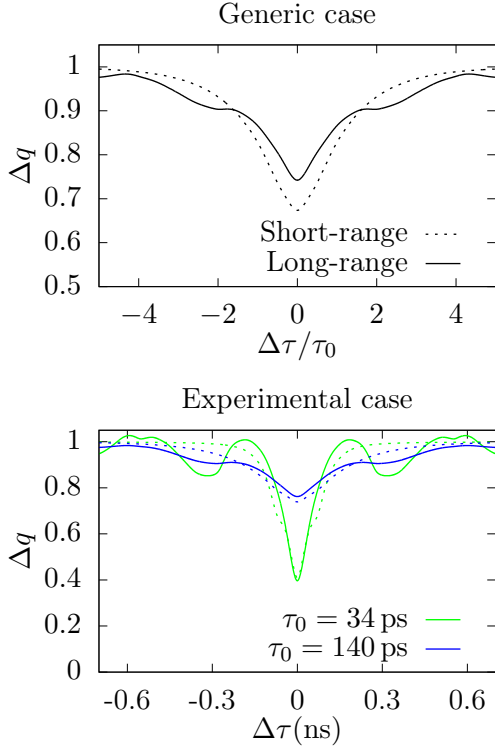


FIG. 17: (Color online) Top panel: Predicted results of an Hong-Ou-Mandel experiment after an interaction region in the short- and long-range cases, at  $\nu = 2$ . The interaction parameters are the ones given in the caption of Fig. 16 and corresponds to interaction region of the same lengths and with the same low energy behaviour in terms of velocities. The main difference between the predictions of the two models are the depth of HOM dip at  $\Delta\tau = 0$  and the secondary dips at  $\Delta\tau = \pm 1.5\tau_0$  in the long-range case which are due to low energy side excitations seen on Fig. 16. The wider time spreading of the outgoing coherence also leads to a wider HOM dip. Bottom panel: Plot of the HOM curves for the long (full lines) and short range (dotted lines) models with parameters corresponding to the experiment<sup>9</sup>.

## A. Magnetoplasmon scattering

### 1. Time domain

Let us start by analyzing what happens to a percussional voltage pulse  $V(t) = V_0\delta(t - t_0)$  sent across this type of interaction zone. The outgoing voltage pulse can be obtained from the inverse Fourier transform of  $t(\omega)$ . Using equation (16), we can rewrite the transmission coefficient in the generic case as

$$t(\omega) = S_{11}(\omega) \quad (41a)$$

$$+ e^{i\omega\tau_L} S_{12}(\omega) S_{21}(\omega) \sum_{n=0}^{\infty} e^{in\omega\tau_L} S_{22}(\omega)^n \quad (41b)$$

This expression has a clear physical meaning. Indeed, all excitations recovered in channel 1 after the interac-

tion region of size  $l$  correspond to one of the following paths: term (41a) correspond to incoming excitations directly crossing the region in channel 1 whereas terms (41b) corresponds to incoming excitations generating excitations in channel 2 ( $S_{21}$ ) which go round the closed loop and create excitations back in channel 1 ( $S_{12}$ ). This can either happen after one lap round the loop ( $e^{i\omega\tau_L}$ ) or after  $n + 1$  laps, in which case we need to take into account the fact that excitations in channel 2 crossed the interaction region in the second channel  $n$  times ( $S_{22}^n$ ) and made  $n$  more laps ( $e^{in\omega\tau_L}$ ).

In the case of short-range interactions,  $t(\omega)$  can be rewritten as a sum of complex exponentials

$$t(\omega) = p_+ e^{i\omega\tau_+} + p_- e^{i\omega\tau_-} \quad (42)$$

$$+ \sum_{n=0}^{\infty} \sum_{k=0}^{n+2} w_{n,k} e^{i\omega((n+1)\tau_L + k\tau_+ + (n+2-k)\tau_-)}$$

where the weights  $w_{n,k}$  are given by<sup>76</sup>

$$w_{n,k} = q^2 \left[ \binom{n}{k} p_+^{n-k} p_-^k + \binom{n}{k-2} p_+^{n+2-k} p_-^{k-2} - 2 \binom{n}{k-1} p_+^{n+1-k} p_-^{k-1} \right] \quad (43)$$

This equation shows that the outgoing voltage for a localized excitation of charge  $-e$  created at time  $t_0$  corresponds to the generation of a percussional current pulse with charge  $-ep_+$  emitted at time  $t_0 + \tau_+$ , another one with charge  $-ep_-$  at time  $t_0 + \tau_-$ , and an infinity of others at times  $t_0 + (n+1)\tau_L + k\tau_+ + (n+2-k)\tau_-$  with charges  $-ew_{n,k}$ . Total current is conserved, since  $p_+ + p_- = 1$  and  $\forall n, \sum_{k=0}^{n+2} w_{n,k} = 0$ .

For the Leviton source, with the exact same reasoning, the outgoing state is a sum of time-shifted Leviton excitations with suitable charges. Fig. 18 shows the outgoing current for this type of environment computed in two different ways. The top panel of Fig. 18 corresponds to an analytical computation of the expected current in the way we just exposed. The bottom panel is obtained from our numerical code used to compute the outgoing single-electron coherence, by integrating the resulting excess Wigner distribution function over the energy. The very good agreement between the two results illustrates the validity of our numerical approach.

### 2. Frequency domain

Let us now turn to the transmission coefficient as a function of energy. As stated before, since  $|t(\omega)|^2 = 1$ , this system behaves as an effective  $\nu = 1$  system but it has a much richer texture than the model presented in Sec. II C 2.

First of all, let us consider short-range interactions at weak coupling. The closed inner channel can be seen as a Fabry-Pérot interferometer with low transparency



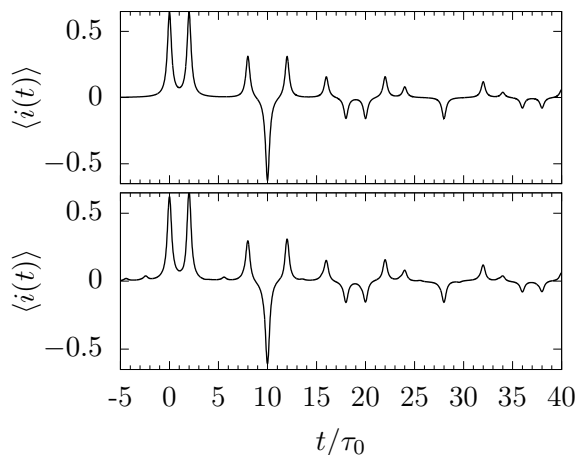


FIG. 18: Outgoing current for an incoming leviton excitation of width  $\tau_0/4$  after an interaction with a closed loop. Parameters  $\tau_- = \tau_0$ ,  $\tau_+ = 3\tau_0$  and  $\tau_L = 7\tau_0$ . Such parameters, while not experimentally reasonable, allow a good visualization of the physical properties of this current. Indeed, we see first the two peaks corresponding to standard fractionalization when crossing the interaction region, followed by a series of three peaks corresponding to excitations having crossed two times the interaction region and going round the loop once (first corresponds to two crossings in the symmetric mode, then one antisymmetric and one symmetric, third one is two crossings in antisymmetric mode), and so on. Top panel: as given by the analytical computation presented in this section. Bottom panel: as recovered when integrating the numerically obtained outgoing Wigner function over all energies.

on one side and totally reflecting on the other part. The interaction region can then be viewed as a cavity which is connected to a transmission line. As in optics, the phase of its reflexion coefficient, which is here the edge-magnetoplasmon transmission  $t(\omega)$ , exhibits sharp resonances. They can arise from quasi-bound scattering states within the interaction region seen as a cavity, which appear as peaks in the Wigner-Smith time delay

$$\tau_{\text{WS}}(\omega) = \frac{1}{2\pi i} \frac{d \log(t(\omega))}{d\omega} \quad (44)$$

which represents a dwelling time within the cavity. These resonances are sharply visible in the weak-coupling regime presented on Fig. 19. The top panel depicts the phase of  $t_{\text{eff}}(\omega) = e^{-i\omega\tau_-} t(\omega)$ , and displays strong jumps of  $2\pi$  every time  $\omega(\tau_+ + \tau_L) \simeq 2n\pi$ . These jumps lead to strong resonances in the Wigner Smith time delay as seen on the lower panel.

Let us now turn to the strong-coupling case ( $\theta = \pi/2$ ). As is expected from the comparison with a Fabry-Pérot interferometer with higher transparency, the quasi bound states inside the loop are broadened in energy, as can be seen on Fig. 20.

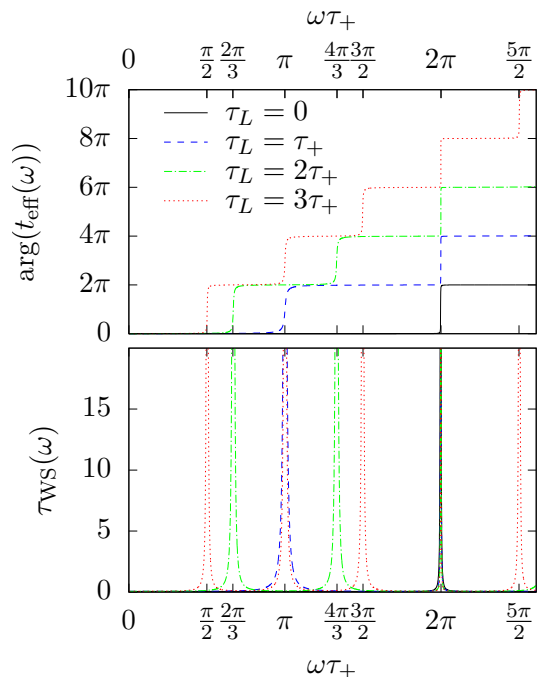


FIG. 19: (Color online) Phase of the transmission coefficient (top panel) and the associated dwelling time  $\tau_{\text{WS}}(\omega)$  (lower panel) for a short-range interaction with weak coupling ( $\theta = \pi/10$ ) and parameters  $\tau_- = \tau_+/20$ , for 4 different geometries for the loop. We see that the phase jumps each time  $\omega(\tau_+ + \tau_L) \simeq 2n\pi$ , with a stronger jump when  $\omega\tau_+ = 2\pi$ . These jumps are the signature of a quasi bound state (scattering resonance) at corresponding energy inside the loop.

## B. Electronic decoherence

We now discuss electronic relaxation and decoherence of Landau excitations at strong coupling in the closed channel geometry depicted on Fig. 6(a) ( $\tau_L = 0$ ). Numerical results for the Wigner function of an electron emitted below the energy of the first resonance of the closed resonator and one emitted between the first and the second resonances are shown on the upper panels of Figs. 21 and 22. These results are compared, on the bottom panel of each figure, to a situation where the interaction region is of the same length but the inner channel is not closed onto itself. The geometry with a closed channel exhibit much less electronic decoherence in comparison with the open channel geometry.

In the first situation depicted on Fig. 21, electron/hole pair generation is inhibited because the electronic energy is off resonance with the cavity and therefore, relaxation is blocked. As a result, no decoherence happens and the excitation leaves the interaction region pretty much unchanged.

When the Landau excitation is injected above the first resonance (see upper panel of Fig. 22), it relaxes by emit-

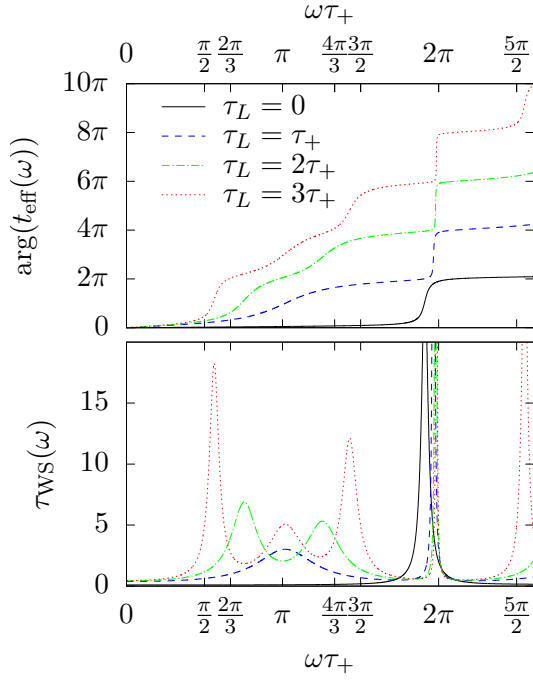


FIG. 20: (Color online) Phase of the transmission coefficient (top panel) and associated dwelling time in the closed inner channel (lower panel) for a short-range interaction with strong coupling ( $\theta = \pi/2$ ) and the same 4 different geometries for the loop as the low-coupling case. We see that the phase does not go from one plateau to another, but still exhibits jumps at values close to the ones seen before, the jump at  $\omega\tau_+ = 2\pi$  being once again the strongest. The corresponding quasi bound states inside the loop are therefore broadened in energy.

ting electron/hole pairs precisely at the energy given by the first resonance. This relaxation leads to a peak in the electronic distribution at the final energy of the electron, which is its injection energy minus the resonance energy. The characteristic features of the interaction-generated electron/hole pair cloud are the temporal oscillations of  $\Delta\mathcal{W}^{(e)}(t, \omega)$  for  $\omega$  below the peak associated with the relaxed electron. HOM interferometry can then be used to check whether or not we are protected against decoherence. As shown on Fig. 23, the HOM dip for wavepackets propagating along a closed inner channel should be bigger than their opened counterpart, going even down close to zero for an excitation emitted below the first resonance.

### C. A realistic sample proposal

In this section, we discuss a possible geometry in which Landau excitations such as the one emitted by a single-electron source<sup>14</sup> would be protected against decoherence.

One may naively think that loops smaller than the

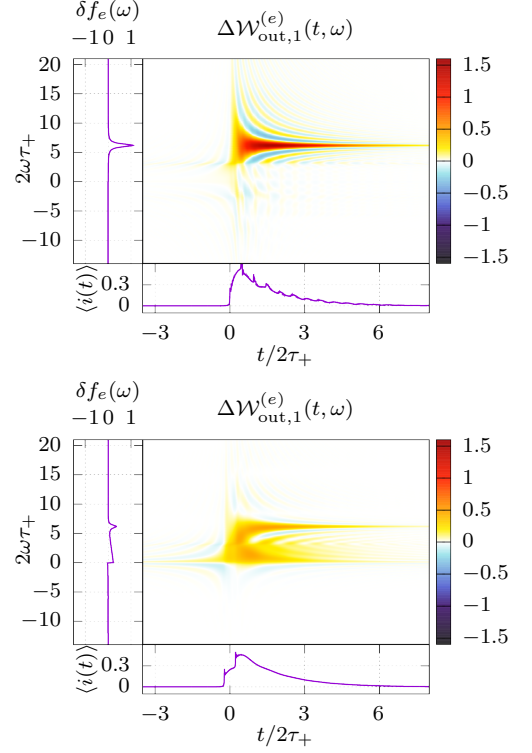


FIG. 21: (Color online) Outgoing Wigner function for an incoming Landau excitation of duration  $\tau_0 = 0.8\tau_+$ . Interaction parameters are  $\theta = \pi/2$  and  $\tau_- = \tau_+/10$ . Top panel: short-range interaction with a closed environment of type (a) ( $\tau_L = 0$ ). Bottom panel: copropagation along an open channel on the same distance with same interaction parameters. For both graphs, the incoming excitation is at an energy  $\omega_0\tau_+ = \pi$  below the energy resonances of the loop. When interacting with a closed channel (upper panel), relaxation is highly suppressed compared to copropagation along an open channel (lower panel). Because the injection energy is below closed channel resonances, the outgoing occupation number remains close to the incoming one. Electron/hole pair creation is responsible of the spikes that appear on the average electric current which are characteristic of the closed channel geometry.

size of dots used to emit the excitation would be needed, which seems unreasonable experimentally. Luckily, previous experimental studies<sup>69</sup> have shown that the speed of electronic excitations in top-gated regions of the 2DEG are smaller than the “free” velocity, a fact that can be checked using available experimental data on the energies of the quantum dot. The energy  $\hbar\omega_0$  of Landau particles emitted by the dot used in Ref.<sup>9</sup> is around 60  $\mu\text{eV}$ , the size of the dot being 2  $\mu\text{m}$ , leading to a relevant velocity in gated region of the 2DEG  $v^{\text{gate}} \sim 5.8 \times 10^4 \text{ m s}^{-1}$ . The dwelling time of excitations in the dot is  $\tau_0 \simeq 100 \text{ ps}$ , leading to a typical width in energy of about 1/10th of the injection energy. Consequently, a safe limit for blocking decoherence would be to have a loop such that  $\omega_0(\tau_+ + \tau_L) < 3\pi/2$ . The edge-magnetoplasmon modes populated within the incoming electronic excita-

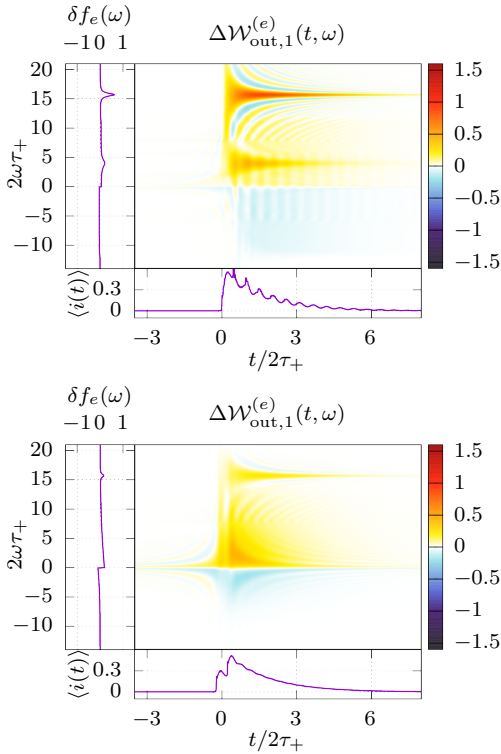


FIG. 22: (Color online) Same as Fig. 21, but for an incoming excitation above the resonance energy,  $\omega_0\tau_+ = 5\pi/2$ . Energy relaxation involves the emission of electron/hole pairs at the resonance energy, leading to a second peak in the energy distribution.

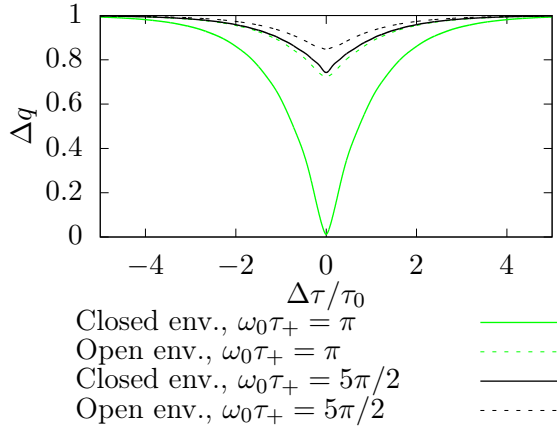


FIG. 23: (Color online) Results of an Hong-Ou-Mandel experiment for the 4 Wigner distributions presented in this section. The bigger depth of the HOM dip for the loop environment proves that closing the environment on itself provides a net advantage compared to the open case. Specifically, in the case where the excitation is emitted below the first level in the loop ( $\omega\tau_+ = \pi$ ), we see a dip going nearly all the way down to 0, which denotes a quasi-complete protection from decoherence.

tions have their energies below the resonance, even when considering the resonance width.

A sample design with a loop of total size  $4\mu\text{m}$  is sketched on Fig. 24. We predict protection against decoherence for the single-electron excitations we are interested in. Of course, by tuning the dot parameters for emitting excitations at lower energies, decoherence protection would still be possible even with two times larger loops (see Appendix G, Fig. 27). The design presented here would allow a test of decoherence protection for single-electron excitations emitted by the mesoscopic capacitor driven by square pulses. Electronic decoherence and relaxation of energy resolved single-electron excitations being stronger than for an out of equilibrium distribution generated by a biased QPC, such an experiment would provide a stronger test of the potential of sample design for decoherence protection.

Finally, as was presented on Fig. 22, larger loops with  $2\pi \leq \omega_0(\tau_+ + \tau_L) \leq 4\pi$  give access to the physics of electronic excitations accompanied by a single plasmon around an energy given by the first scattering resonance of the loop. This allows the probing of new hybrid quantum single-electron and single-plasmon excitations and calls for new protocol measurements to fully characterize these excitations.

## V. CONCLUSION

To conclude, we have addressed the question of decoherence control for single-electron excitation propagating within chiral edge channels. This work is focused on purely passive decoherence control through the properties of the material itself and sample design.

To get an insight on the influence of the material, we have discussed electronic decoherence within an ideal single chiral channel. Using a semi-realistic model for long-range interactions, we have found that a high bare Fermi velocity may be significantly more promising for limiting decoherence because it leads to a lower coupling constant, a point that has indeed been overlooked, and because it amplifies the distance covered within a given time. We have found that the conjugation of these two effects could lead to a drastic decrease of electronic decoherence over distances of 10 to  $100\mu\text{m}$  as long as dissipative effects could be neglected. We think that this calls for more thorough experimental studies to explore the potential of different materials for electron quantum optics. Moreover, our analysis once again stresses the importance of performing electronic decoherence experiments in setups where finite-frequency a.c. transport could also be measured.

We have also shown that passive decoherence protection through sample design could be tested for excitations emitted by the mesoscopic capacitor in the single-electron regime using an HOM experiment. We have proposed a realistic design for demonstrating this effect. Moreover, our study suggests that such sample could be used for

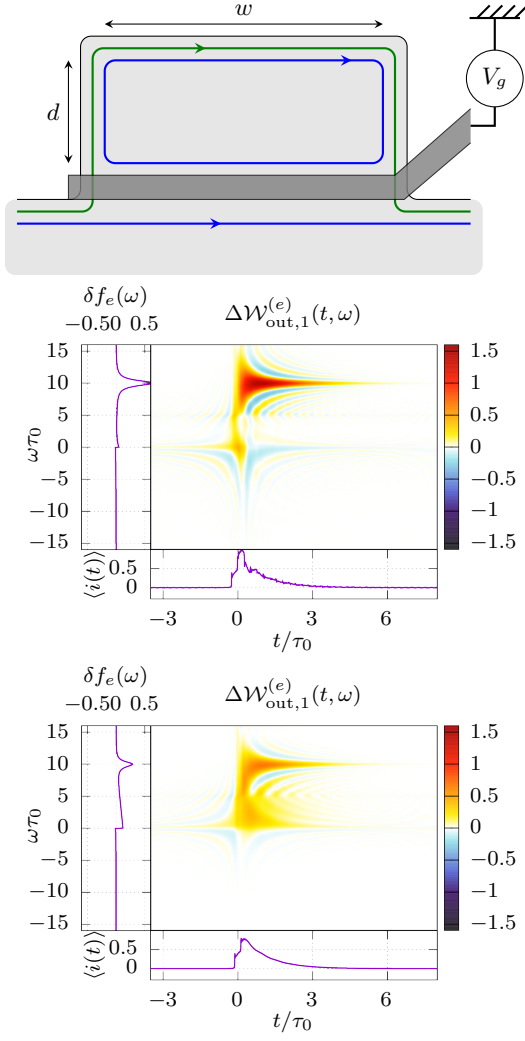


FIG. 24: (Color online) Top panel: a possible experimental design for testing decoherence control on a Landau excitation. Here, the 2DEG (in light gray) defines a cavity delimited by a top gate shifting the electron density so that only the outer edge channel can pass through. This creates a region with a closed inner channel. The single-electron source as well as the QPC of the HOM probe should be located close to the loop. The loop corresponds to  $\tau_+ = (w + 2d)/v_+^{\text{chem.}}$  and  $\tau_L = w/v_F^{\text{gate}}$ , where  $v_+^{\text{chem.}}$  denotes the speed of the slow mode in chemically defined edge channels, whereas  $v_F^{\text{gate}}$  is the Fermi velocity in an edge channel propagating along a metallic gate. Middle panel: outgoing Wigner function when  $w = 1.5 \mu\text{m}$ ,  $h = 0.5 \mu\text{m}$  for an incoming excitation with parameters  $\omega_0\tau_0 = 10$  and  $\tau_0 = 100 \text{ ps}$ . The velocities are  $v_+^{\text{chem.}} = 1 \times 10^5 \text{ m s}^{-1}$  and  $v_F^{\text{gate}} = 5.8 \times 10^4 \text{ m s}^{-1}$ . Bottom panel: Wigner function in the case where the gate closing the loop is used to either let both channels through or none (times of flight are equivalent in those two cases). Decoherence would be far more important in such cases where the inner channel is not closed on itself.

emitting single edge magnetoplasmons thus opening the way to hybrid electron-and-photon quantum optics.

## Appendix A: Bosonization

Bosonization provides a description of a 1D chiral relativistic gaz of fermions in terms of bosonic degrees of freedom corresponding to charge density waves. At a given chemical potential  $\mu$ , the excess charge density  $n(x, t)$  is the normal ordered product  $:(\psi^\dagger\psi): (x)$  with respect to the corresponding Fermi energy. It is expressed in terms of a quantum bosonic field  $\phi$

$$:(\psi^\dagger\psi): (x, t) = \frac{1}{\sqrt{\pi}} (\partial_x\phi)(x, t) \quad (\text{A1})$$

whose mode decomposition can be written in terms of creation  $b^\dagger(\omega)$  and destruction operators  $b(\omega)$  called edge-magnetoplasmon modes

$$\phi(x, t) = \frac{-i}{\sqrt{4\pi}} \int_0^{+\infty} \left( b(\omega) e^{i\omega(x/v_F - t)} - \text{h.c.} \right) \frac{d\omega}{\sqrt{\omega}}. \quad (\text{A2})$$

where  $v_F$  denotes the Fermi velocity of fermionic excitations in this chiral channel. The edge-magnetoplasmon modes can be expressed in terms of the fermionic mode operators  $c(\omega)$  and  $c^\dagger(\omega)$  defined by

$$\psi(x, t) = \int_{-\infty}^{+\infty} c(\omega) e^{i\omega(x/v_F - t)} \frac{d\omega}{\sqrt{2\pi v_F}} \quad (\text{A3})$$

through

$$b^\dagger(\omega) = \frac{1}{\sqrt{\omega}} \int_{-\infty}^{+\infty} c^\dagger(\omega + \omega') c(\omega') d\omega'. \quad (\text{A4})$$

This immediately shows that  $b^\dagger(\omega)$  creates a coherent superposition of electron/hole pairs with energy  $\hbar\omega$ . Using Eq. (A1), the finite-frequency modes of the excess electronic current  $i(x, t) = -ev_F n(x, t)$  are directly proportional to the edge-magnetoplasmon modes,  $i(\omega > 0) = -e\sqrt{\omega} b(\omega)$ . The electronic operator can be expressed in terms of these bosonic modes through

$$\psi(x, t) = \frac{\mathcal{U}}{\sqrt{2\pi a}} \exp\left(i\sqrt{4\pi}\phi(x, t)\right) \quad (\text{A5})$$

where  $a$  is an ultraviolet cutoff that gives the length scale below which bosonization is not valid and  $\mathcal{U}$  (resp.  $\mathcal{U}^\dagger$ ) is the ladder operator suppressing (resp. adding) one electron from the reference vacuum.

The fermionic operator  $\psi^\dagger(x, t)$  thus performs two things: it shifts the vacuum state to add one electronic charge  $-e$  to it and then it acts as a displacement operator on the edge-magnetoplasmon modes with parameter  $\Lambda_\omega(x, t) = e^{-i\omega(x/v_F - t)}/\sqrt{\omega}$ :

$$D[\Lambda(x, t)] = \exp\left(\int_0^{+\infty} (\Lambda_\omega(x, t) b^\dagger(\omega) - \text{h.c.}) d\omega\right). \quad (\text{A6})$$

As discussed in Ref.<sup>41</sup>, a classical time-dependent voltage drive  $V(t)$  generates an edge-magnetoplasmon coherent state with parameter  $\Lambda_\omega[V(t)] = -e\tilde{V}(\omega)/h\sqrt{\omega}$ . The coherent state of parameter  $\Lambda_\omega(x, t)$  thus corresponds to the single-electron state generated by a voltage pulse  $V(t) = -(h/e)\delta(t - x/v_F)$  generating a percussional current pulse carrying a single-electron charge.

### Appendix B: A long-range model for $\nu = 1$

In this section, we derive an exact expression for the edge-magnetoplasmon transmission coefficient in the  $\nu = 1$  case using a simple model of Coulomb interaction based on discrete elements in the spirit of Büttiker's treatment of high frequency quantum transport<sup>57</sup>. Electrons within the interaction region see the electric potential  $U(x, t)$  given by a capacitive coupling inside a finite length region of size  $l$ :

$$U(x, t) = \begin{cases} 0 & \text{if } x \notin [-\frac{l}{2}, \frac{l}{2}] \\ \frac{1}{C} \int_{-\frac{l}{2}}^{\frac{l}{2}} n(y, t) dy & \text{else.} \end{cases} \quad (\text{B1})$$

where the excess density of charges  $n$  is itself linked to the bosonic field  $\phi$  through equation (A1). Eq. (5) can be recasted as a closed equation on  $\phi$  expressed in the frequency domain as

$$(-i\omega + v_F \partial_x) \phi(x, \omega) = \frac{e^2}{hC} \left( \phi\left(-\frac{l}{2}, \omega\right) - \phi\left(\frac{l}{2}, \omega\right) \right). \quad (\text{B2})$$

Expressing  $\phi(x, \omega)$  as  $e^{i\omega x/v_F} \varphi_\omega(x)$  leads to

$$\partial_x \varphi_\omega(x) = \frac{e^2}{v_F h C} e^{-i\omega x/v_F} \left( e^{-i\omega l/(2v_F)} \varphi_\omega\left(-\frac{l}{2}\right) - e^{i\omega l/(2v_F)} \varphi_\omega\left(\frac{l}{2}\right) \right) \quad (\text{B3})$$

which can be integrated over the whole interaction region to give us a relation between  $\varphi_\omega(-\frac{l}{2})$  and  $\varphi_\omega(\frac{l}{2})$ . Finally, the solution reads

$$\phi\left(\frac{l}{2}, \omega\right) = t(\omega) \phi\left(-\frac{l}{2}, \omega\right) \quad (\text{B4})$$

where

$$t(\omega) = e^{i\omega l/v_F} \frac{1 + A(\omega, l)e^{-i\omega l/(2v_F)}}{1 + A(\omega, l)e^{i\omega l/(2v_F)}} \quad (\text{B5a})$$

$$A(\omega, l) = \frac{4e^2/C}{hv_F/l} \text{sinc}\left(\frac{\omega l}{2v_F}\right) \quad (\text{B5b})$$

in which we recognize the kinetic energy scale  $hv_F/l$  as well as the dimensionless ratio  $\alpha = e^2 l / Chv_F$  of the electrostatic energy  $e^2/C$  to this kinetic energy scale, which quantifies the strength of Coulomb interactions in this system. Note that, at least for sufficiently long edge channels, this coupling constant does not depend on the length  $l$  since  $C$  also scales as  $l$ .

As expected, the transmission coefficient  $t(\omega)$  is of modulus 1 because no energy can be lost in a  $\nu = 1$  setup without any dynamical environment. The quantity of interest is therefore the phase of  $t(\omega)$ .

In the limit where Coulomb interaction effects can be neglected ( $\alpha \rightarrow 0$ ),  $t(\omega) = e^{i\omega l/v_F}$  showing that the bare Fermi velocity is recovered. The opposite limit of ultra-strong Coulomb interactions ( $\alpha \rightarrow \infty$ ) leads to  $t(\omega) = 1$ , that is an infinite edge-magnetoplasmon velocity. However, at fixed coupling  $\alpha$ , the edge-magnetoplasmon velocity tends to  $v_\infty = v_F$  when  $\omega l/v_F \gg 1$ . At low frequency, we find that the time of flight of edge magnetoplasmons is renormalized thus leading to an increased renormalized plasmon velocity

$$\frac{v_0}{v_\infty} = 1 + \frac{4e^2/C}{hv_\infty/l}. \quad (\text{B6})$$

compared to the velocity at high frequency which is the bare Fermi velocity  $v_F$ .

To estimate an order of magnitude of this ratio, let us remind that  $C$  being the capacitance of the interaction region that is roughly similar to a 1D wire,  $C \simeq 2\pi\epsilon_0\epsilon_r l$  up to a geometrical factor for large  $l$ , that is when boundary effects are small. Consequently,  $\alpha$  does not depend on  $l$  but behaves as<sup>41</sup>:

$$\alpha \simeq \frac{\alpha_{\text{qed}}}{\pi\epsilon_r} \times \frac{c}{v_F} \times (\text{Geometrical Factor}) \quad (\text{B7})$$

where  $\alpha_{\text{qed}}$  denotes the fine-structure constant,  $\epsilon_r$  the relative permittivity of the material and  $v_F$  the bare Fermi velocity.

For AsGa, one usually estimates  $v_F \simeq 10^5$  m/s and  $\epsilon_r \simeq 10$  thus leading to

$$\alpha \simeq 0.75 \times (\text{Geometrical Factor}) \quad (\text{B8})$$

Assuming a geometrical factor of order 1, this gives a velocity for low-energy magnetoplasmons of the order of  $v_0 \sim 4 \times 10^5$  m/s which is compatible to what is observed in  $\nu = 2$  edge channel systems<sup>70</sup>. Let us remind that the edge-magnetoplasmon velocity depends on the details of the electric potential seen by electrons near the edge of the 2DEG and therefore of the conception of the sample. This is precisely used in the above reference to modulate it by polarising gates.

In the case of graphene, a common estimation for the Fermi velocity is of the order of  $v_F \simeq 1 \times 10^6$  m/s and  $\epsilon_r \simeq 14$ <sup>54,71</sup> thus leading to

$$\alpha \simeq 0.054 \quad (\text{B9})$$

when using a geometrical factor equal to unity. The coupling constant is much lower and therefore  $v_0/v_F \simeq 1.2$ . Let us stress that, as far as we know, no direct measurement of  $v_F$  in quantum Hall edge channels of graphene have been performed but if this commonly discussed value is confirmed, this would put graphene in a totally different coupling range than AsGa.

For intermediate values of the coupling constant  $\alpha$ , as shown on Fig. 5, the edge-magnetoplasmon velocity deduced from  $t(\omega)$  presents a decay from  $v_0$  to a regime with small oscillations above the asymptotic value of  $v_F$ .

Expanding the phase of  $t(\omega)$  in powers of  $\omega\tau_0$  leads to

$$\begin{aligned} \phi(\omega) &= \omega\tau_0 + \frac{\alpha}{3}(\omega\tau_0)^3 \\ &+ \frac{8\alpha}{90}(\alpha^2 + 2\alpha - 1/8)(\omega\tau_0)^5 + \mathcal{O}((\omega\tau_0)^7) \end{aligned} \quad (\text{B10a})$$

which, as explained Appendix F, gives us the low energy expansion of the inelastic scattering probability.

### Appendix C: Energy dissipation

Let us discuss energy dissipation through the creation of electron/hole pairs in the  $\nu = 1$  case. To begin with, this discussion makes sense when there is a clear separation in energy between the injected electron after relaxation and the electron/hole excitations generated by Coulomb interaction (see Sec. III C 1). In the following discussion, we shall thus assume that the spectral weight of the incoming electron as well as of the contribution  $\mathcal{G}_{\text{WP},1}^{(e)}$  to the outgoing coherence are well above the vicinity of the Fermi level.

The incoming average energy comes from the injected electron and is equal to

$$E_{\text{in}} = \hbar \int_0^{+\infty} |\tilde{\varphi}_e(\omega)|^2 \omega \frac{d\omega}{2\pi v_F}. \quad (\text{C1})$$

using the convention

$$\tilde{\varphi}_e(\omega) = v_F \int_{-\infty}^{+\infty} \varphi_e(-v_F t) e^{i\omega t} dt \quad (\text{C2})$$

for defining the electronic wavepacket in the frequency domain from the original wavefunction  $\varphi_e$  in the spatial domain.

The outgoing average energy then consists of two parts: the energy carried by the injected electron which has flown across the interaction region either elastically or inelastically, and the energy of electron/hole excitations created by its passing through. The first contribution is

$$E_{\text{out}}^{(e)} = Z_{\infty} E_{\text{in}} \quad (\text{C3a})$$

$$+ \hbar \int_{(\mathbb{R}^+)^2} |\varphi_e(\omega)|^2 (\omega - \omega') d(\omega') d\omega' \frac{d\omega}{2\pi v_F} \quad (\text{C3b})$$

The first line corresponds to elastic scattering and the second line to inelastic processes in which the electron has fallen down from  $\hbar\omega$  to  $\hbar(\omega - \omega')$ . There, the integrals are extended to  $+\infty$  safely because of our working hypothesis: the relaxation tail is well above the Fermi level. We then use that  $\int_0^{+\infty} d(\omega') d\omega' = 1 - Z_{\infty}$  and the

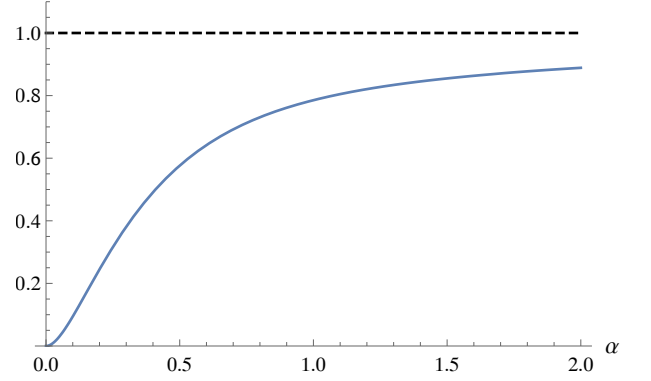


FIG. 25: Dependence on the coupling constant  $\alpha$  of  $E_{\text{out}}^{(\text{diss})}(\alpha, hv_F/l)$  in units of  $hv_0/l$  where  $E_{\text{out}}^{(\text{diss})}(\alpha, hv_F/l)$  denotes the average energy dissipated by a hot electron given by Eq. (C7) corresponding to the model discussed in Appendix B.

normalization condition of the wavepacket to rewrite this as

$$E_{\text{out}}^{(e)} = E_{\text{in}} - \hbar \int_0^{+\infty} \omega' d(\omega') d\omega' \quad (\text{C4})$$

Energy conservation, which is true on average, shows that the dissipated energy in electron/hole pair creation is equal to

$$E_{\text{out}}^{(\text{diss})} = \hbar \int_0^{+\infty} \omega d(\omega) d\omega \quad (\text{C5})$$

Recognizing that  $\int_0^{+\infty} \omega d(\omega) d\omega$  corresponds to the derivative of the decoherence coefficient  $\mathcal{D}(\tau)$  when  $\tau \rightarrow 0^+$  leads to

$$E_{\text{out}}^{(\text{diss})} = \hbar \int_0^{+\infty} |1 - \tilde{t}(\omega)|^2 d\omega. \quad (\text{C6})$$

Using the transmission coefficient given by Eq. (B5), the dissipated energy is given by

$$E_{\text{out}}^{(\text{diss})} = \frac{hv_F}{\pi l} \int_0^{+\infty} \frac{64\alpha^2 \sin^4(u) du}{(u + 2\alpha \sin(2u))^2 + 16\alpha^2 \sin^2(u)}. \quad (\text{C7})$$

which converges both in the UV and the IR.

Fig. 25 presents the numerical evaluation of the dissipated energy in units of  $hv_0/l$ , where  $v_0 = (1 + 4\alpha)v_F$  is the low energy edge-magnetoplasmon velocity in this model. We observe that it saturates to 1 at large coupling. The finiteness of the dissipated energy validates a posteriori that the high-energy description of electronic decoherence is valid as long as the average energy of the incoming excitation is large compared to  $\alpha hv_0/l$ .

As a final check, one can rederive Eq. (C6) by considering the reduced density operator for the low energy electron/hole pair excitations. When assuming that even after relaxation, the wavepacket remains well

separated from the Fermi sea, one can assume that  $\langle \psi(t_-)\psi^\dagger(t_+) \rangle_F \simeq v_F^{-1}\delta(t_+ - t_-)$  in (27a) and therefore  $\mathcal{G}_{\text{MV},1}^{(e)}(t|t')$  can be approximated by an expression which corresponds to the statistical mixture of states  $|g(t)\rangle$  ponderated by  $|\varphi_e(t)|^2$ . This naturally comes from the physical image of the incident electron emerging from the interaction in a quantum superposition of the coherent electron/hole pair clouds  $|g(t)\rangle$  attached to the electron being at position  $v_F t$ . Two different positions  $v_F t$  and  $v_F t'$  of the electron being perfectly distinguishable, what comes out is the statistical mixture of coherent electron/hole pair clouds for the low energy edge-magnetoplasmon modes. Computing the average energy stored in this statistical mixture precisely leads to (C6) since all the states  $|g(t)\rangle$  carry the same average energy.

#### Appendix D: Discrete element circuit description

In this appendix, we discuss the circuit synthesis for the edge-magnetoplasmon transmission amplitude in the case of an ideal  $\nu = 1$  edge channel and we obtain its first non trivial Cauer form. We then connect the discrete circuit element parameters to the parameters of the model presented in Appendix B.

##### 1. Circuit synthesis for an ideal $\nu = 1$ edge channel

Using the relation  $t(\omega) = 1 - R_K G(\omega)$  where  $G(\omega)$  is the finite-frequency admittance of the discrete element circuit of Fig. 7, the transmission amplitude  $t(\omega)$  can be expressed in terms of the impedance  $Z(\omega)$  as

$$t(\omega) = \frac{1 + \omega C_\mu \Im(Z(\omega)) + i\omega C_\mu (R_K - \Re(Z(\omega)))}{1 + \omega C_\mu \Im(Z(\omega)) - i\omega C_\mu \Re(Z(\omega))}. \quad (\text{D1})$$

Consequently,  $t(\omega)$  is a pure phase if and only if  $\Re(Z(\omega)) = R_K/2$  at all frequencies. We can then write

$$t(\omega) = \frac{1 + i\alpha(\omega)}{1 - i\alpha(\omega)} = \exp(2i \arctan(\alpha)) \quad (\text{D2})$$

where

$$\alpha(\omega) = \frac{\omega R_K C_\mu}{2} \frac{1}{1 + \omega C_\mu \Im(Z(\omega))}. \quad (\text{D3})$$

With our conventions, the reactance  $\Im(Z(\omega))$  is a strictly decreasing function of  $\omega$ <sup>72</sup>. Since, by definition, the electrochemical capacitance  $C_\mu$  contains the low-frequency divergence of the ZC circuit, it is expected to be regular at low frequency, starting with a zero at  $\omega = 0$  and then alternating poles and zeroes. A suitable low-frequency expansion of  $t(\omega)$  can then be obtained using a Cauer form of circuit synthesis which leads to a continuous fraction expansion of the finite-frequency admittance.

The simplest case corresponds to the circuit depicted on the right panel of Fig. 7. It leads to

$$\alpha(\omega) = \frac{\omega R_K C_\mu}{2} \frac{1 - \omega^2 LC}{1 - \omega^2 L(C + C_\mu)} \quad (\text{D4})$$

Expanding  $2 \arctan(\alpha(\omega))$  in powers of  $\omega R_K C_\mu$  then leads to the low-frequency finite-frequency admittance up to order  $(\omega R_K C_\mu)^6$ :

$$g(\omega) = -i\omega R_K C_\mu + \frac{1}{2}(\omega R_K C_\mu)^2 \quad (\text{D5a})$$

$$- i \left[ \frac{L/R_K}{R_K C_\mu} - \frac{1}{4} \right] (\omega R_K C_\mu)^3 \quad (\text{D5b})$$

$$+ \left[ \frac{L/R_K}{R_K C_\mu} - \frac{1}{8} \right] (\omega R_K C_\mu)^4 \quad (\text{D5c})$$

$$- i \left[ \left( 1 + \frac{C}{C_\mu} \right) \left[ \frac{L/R_K}{R_K C_\mu} \right]^2 + \frac{1}{16} - \frac{3}{4} \frac{L/R_K}{R_K C_\mu} \right] (\omega R_K C_\mu)^5 \quad (\text{D5d})$$

which then leads to Eqs. (39).

Being described by two parameters ( $L$  and  $C$ ) besides  $C_\mu$  and  $R_q = R_K/2$ , this circuit provides an expansion of  $\phi(\omega)$  up to order  $(\omega R_K C_\mu)^5$ . In order to capture the low-frequency behavior of  $\phi(\omega)$  to the next non trivial orders (7 and 9), we need to go one step further in the Cauer form of the circuit. This would correspond to adding another  $LC$  impedance in series with the capacitor  $C$ . This process can then be iterated to reconstruct the full  $\omega$  dependence of  $\Im(Z(\omega))$ .

##### 2. Extracting the discrete element parameters

Let us now derive the discrete element circuit parameters for the interaction model at  $\nu = 1$  considered in Appendix B. Expanding the admittance at low frequency and identifying this expansion with (D5) leads to

$$R_K C_\mu = \tau_0 = l/v_0 \quad (\text{D6a})$$

$$\frac{L/R_K}{R_K C_\mu} = \frac{1 + 4\alpha}{12} \quad (\text{D6b})$$

$$\frac{C}{C_\mu} = \frac{1 + 4\alpha}{5} \quad (\text{D6c})$$

The inductance  $L$  as well as the capacitance  $C$  increase when increasing the effective Coulomb interaction strength. This is expected since increasing Coulomb interactions tend to increase the velocity ratio  $v_0/v_\infty$ . In this model the ratio of  $L/C$  to  $R_K^2$  remains constant and equal to  $5/12$ . Note that for  $L = R_K^2 C_\mu/12$  and  $C = C_\mu/5$ ,  $\alpha_3 = \alpha_5 = 0$ : the first non trivial contribution in  $\phi(\omega)$  appears at order  $(\omega R_K C_\mu)^7$ .

### Appendix E: Phenomenological models for plasmon velocity

Let us discuss problems that arise for some phenomenological expressions for the edge magnetoplasmons in the ideal  $\nu = 1$  case.

We first consider the phenomenological expression

$$\frac{v(\omega)}{v_0} = \frac{1 + \frac{v_\infty}{v_0} (\omega/\omega_c)^2}{1 + (\omega/\omega_c)^2} \quad (\text{E1})$$

which interpolates between  $v_0$  at low frequency and  $v_\infty$  at high frequency, the crossover scale being  $\omega_c$ . We shall denote by  $\tau_0 = l/v_0$ . The finite-frequency admittance only depends on the dimensionless variable  $\omega\tau_0$  and parameters  $0 < v_\infty/v_0 \leq 1$  and  $\omega_c\tau_0 > 0$ . Compared to the long-range interaction model detailed in Appendix B, this phenomenological expression avoids oscillations in the edge-magnetoplasmon velocity and it depends on one more parameter than just  $l/v_0$  and the coupling constant. However, as we will see now, is it not physically acceptable!

A first hint of a problem comes from the low energy expansion using a discrete element circuit description that reproduces the same  $t(\omega)$  dependence up to order 5. Then, under this condition, the electrochemical capacitance  $C_\mu$ , the inductance  $L$  and the capacitance  $C$  of the first ladder in the Cauer expansion are given by:

$$R_K C_\mu = \tau_0 \quad (\text{E2a})$$

$$\frac{L/R_K}{R_K C_\mu} = \frac{1}{12} + \left(1 - \frac{v_\infty}{v_0}\right) \frac{1}{(\omega_c\tau_0)^2} \quad (\text{E2b})$$

$$\frac{C}{C_\mu} = \frac{\frac{1}{720} + \left(1 - \frac{v_\infty}{v_0}\right) \left[ \frac{1}{60(\omega_c\tau_0)^2} - \frac{1}{(\omega_c\tau_0)^4} \right]}{\left[ \frac{1 - \frac{v_\infty}{v_0}}{(\omega_c\tau_0)^2} + \frac{1}{12} \right]^2} \quad (\text{E2c})$$

As expected, the eigenfrequency  $1/\sqrt{LC_\mu}$  corresponds, up to renormalization, to  $\omega_c$ . Since  $v_\infty \leq v_0$  these expressions give a physical value for the inductance  $L$  but  $C/C_\mu$  sometimes becomes negative! This is a serious hint that Eq. (E1) is not a physically meaningful  $\omega$ -dependence for the edge-magnetoplasmon velocity. This can be seen by considering the analytical continuation of  $\Re(1 - t(\omega))$  to the complex plane  $s = \sigma + i\omega$  which must be positive for  $\sigma < 0$ : it exhibits singularities (and thus negativities) on the negative real axis ( $\sigma < 0$  and  $\omega = 0$ ).

In the same way, a phenomenological edge-magnetoplasmon velocity with a sharper high-energy stabilization towards  $v_\infty$  such as<sup>73,74</sup>

$$\frac{v(\omega)}{v_\infty} = 1 + \frac{v_0 - v_\infty}{v_\infty} e^{-(\omega\tau_c)^2}. \quad (\text{E3})$$

is not physical within our framework because the analytical continuation of  $\Re(1 - e^{i\omega l/v(\omega)})$  also presents singularities in the half plane  $\sigma + i\omega$  for  $\sigma < 0$ .

### Appendix F: Low energy perturbative expansion

Here, we consider low energy excitations that have almost all their spectral weight below  $\omega_c$ . The relevant base velocity is  $v_0$  and therefore, we define the effective transmission amplitude as  $\tilde{t}(\omega) = t(\omega) e^{-i\omega\tau_0}$  so that the deviation from  $\tilde{t}(\omega) = 1$  for  $0 < \omega \lesssim \omega_c$  is small.

Assuming that  $\tilde{t}(\omega) = 1$  for  $\omega \lesssim \omega_c$ , the electronic excitation experiences no decoherence for the part which is located below  $\omega_c$ : it simply moves at the plasmon velocity  $v_0$ . This is consistent with the high-energy picture discussed in Sec. III C 1: although a high-energy electronic excitation moves forward at the velocity  $v_\infty$  together with its relaxation tail, the electron/hole pairs created close to the Fermi level move at the plasmon velocity  $v_0$ . The idea is thus to perform a perturbative expansion in terms of  $\omega\tau_0$  of the rescaled edge-magnetoplasmon transmission coefficient  $\tilde{t}(\omega)$ .

At low frequency, the edge-magnetoplasmon transmission coefficient is of the form

$$\tilde{t}(\omega) = \exp\left(i \sum_{k \geq 2} \alpha_k (\omega\tau_0)^k\right) \quad (\text{F1})$$

where  $\tau_0$  is a typical time scale of the problem and  $\alpha_k$  dimensionless couplings. Note that only odd powers of  $\omega\tau_0$  need to be considered because, as discussed in Sec. II C 1,  $t(\omega)^* = t(-\omega)$ .

To obtain the inelastic scattering probability  $\sigma_{\text{in}}(\omega) = 1 - |\mathcal{Z}(\omega)|^2$ , we shall expand perturbatively in  $\omega\tau_0$  the elastic scattering amplitude

$$\mathcal{Z}(\omega) = 1 + \int_0^\omega B_-(\omega') d\omega' \quad (\text{F2})$$

where

$$B_-(\omega) = \sum_{n=1}^{\infty} \frac{1}{n!} \left(\frac{t(\omega) - 1}{\omega}\right)^{*n}(\omega) \quad (\text{F3})$$

is expanded as a series of convolution powers  $(\cdot)^{*n}$ . Denoting  $P(\omega) = \frac{t(\omega)-1}{\omega}$ , we have

$$\begin{aligned} \frac{P(\omega)}{\tau_0} &= i\alpha_3 (\omega\tau_0)^2 + i\alpha_5 (\omega\tau_0)^4 - \frac{\alpha_3^2}{2} (\omega\tau_0)^5 \\ &+ i\alpha_7 (\omega\tau_0)^6 - \alpha_3\alpha_5 (\omega\tau_0)^7 \\ &+ \mathcal{O}\left((\omega\tau_0)^8\right) \end{aligned} \quad (\text{F4a})$$

$$\begin{aligned} \frac{P^{*2}(\omega)}{\tau_0} &= -\frac{\alpha_3^2}{30} (\omega\tau_0)^5 - \frac{2\alpha_3\alpha_5}{105} (\omega\tau_0)^7 \\ &+ \mathcal{O}\left((\omega\tau_0)^8\right) \end{aligned} \quad (\text{F4b})$$

$$\frac{P^{*3}(\omega)}{\tau_0} = \mathcal{O}\left((\omega\tau_0)^8\right) \quad (\text{F4c})$$

Consequently, the expansion of  $\mathcal{Z}(\omega)$  up to order  $(\omega\tau_0)^8$  only involves the 2nd convolution power of  $P$ . This corresponds to two edge-magnetoplasmon emission processes.



Processes with higher multi-plasmon emission will only contribute to higher powers in  $\mathcal{Z}(\omega)$ 's expansion. Limiting ourselves to this order leads to:

$$\begin{aligned} \mathcal{Z}(\omega) = & 1 + \frac{i\alpha_3}{3} (\omega\tau_0)^3 + \frac{i\alpha_5}{5} (\omega\tau_0)^5 \\ & - \frac{31}{360} \alpha_3^2 (\omega\tau_0)^6 + \frac{i\alpha_7}{7} (\omega\tau_0)^7 \\ & - \frac{106}{105} \alpha_3 \alpha_5 (\omega\tau_0)^8 + \mathcal{O}\left((\omega\tau_0)^9\right) \end{aligned} \quad (\text{F5})$$

which gives the final result for the inelastic scattering probability  $\sigma_{\text{in}}(\omega) = 1 - |\mathcal{Z}(\omega)|^2$ :

$$\begin{aligned} \sigma_{\text{in}}(\omega) = & \frac{11\alpha_3^2}{180} (\omega\tau_0)^6 + \frac{5\alpha_3\alpha_5}{42} (\omega\tau_0)^8 \\ & + \mathcal{O}\left((\omega\tau_0)^9\right) \end{aligned} \quad (\text{F6})$$

thus recovering Eq. (38). Note that keeping only the first convolution power in the expansion would lead to

$$\begin{aligned} \sigma_{\text{in}}^{(1)}(\omega) = & \frac{\alpha_3^2}{18} (\omega\tau_0)^6 - \frac{7\alpha_3\alpha_5}{60} (\omega\tau_0)^8 \\ & + \mathcal{O}\left((\omega\tau_0)^9\right) \end{aligned} \quad (\text{F7})$$

which is the inelastic scattering probability arising from single edge-magnetoplasmon emission.

## Appendix G: More experimentally relevant Wigner functions

In this appendix, we show some more Wigner functions for loops built as in Fig. 24 of different sizes, and excitations of different energies. Velocities parameters are the same as in the main text, and Landau excitations have a typical time  $\tau_0 = 100$  ps. All other parameters are shown below the corresponding Wigner functions. On all figures, the top panel shows a closed loop, whereas middle panel shows the case where both edge channels would stay outside of the loop and experience standard interaction along a length  $w$ . The bottom panel then displays the expected results of an HOM experiment for both cases. Using these figures, we can gain a more quantitative understanding of how changing the loop size or the injection energy impacts the experimentally accessible quantities.

### Acknowledgments

We thank C. Bauerle, J.M. Berroir, E. Bocquillon, V. Freulon, F.D. Parmentier, P. Roche and B. Plaças for useful discussions. This work is supported by the ANR grant "1shot reloaded" (ANR-14-CE32-0017) and ERC Consolidator grant "EQuO" (No. 648236).

- 
- <sup>1</sup> C. Bauerle, D.C. Glattli, T. Meunier, F. Portier, P. Roche, P. Roulleau, S. Takada, and X. Waintal (2018), arXiv:1801.07497.
- <sup>2</sup> J. Splettstoesser and R. Haug, eds., *Single-Electron control in Solid State Devices*, vol. 254 (2017).
- <sup>3</sup> E. Bocquillon, V. Freulon, F. Parmentier, J. Berroir, B. Plaças, C. Wahl, J. Rech, T. Jonckheere, T. Martin, C. Grenier, et al., *Ann. Phys. (Berlin)* **526**, 1 (2014).
- <sup>4</sup> A. Bertoni, P. Bordone, R. Brunetti, C. Jacoboni, and S. Reggiani, *Phys. Rev. Lett.* **84**, 5912 (2000).
- <sup>5</sup> R. Ionicioiu, G. Amaratunga, and F. Udrea, *Int. J. Mod. Phys. B* **15**, 125 (2001).
- <sup>6</sup> A. Bertoni, *J. Comput. Electron.* **6**, 67 (2007).
- <sup>7</sup> B. Roussel, C. Cabart, G. Fève, E. Thibierge, and P. Degiovanni, *Physica Status Solidi B* **254**, 16000621 (2017).
- <sup>8</sup> H. Le Sueur, C. Altimiras, U. Gennser, A. Cavanna, D. Maillly, and F. Pierre, *Phys. Rev. Lett.* **105**, 056803 (2010).
- <sup>9</sup> A. Marguerite, C. Cabart, C. Wahl, B. Roussel, V. Freulon, D. Ferraro, C. Grenier, J.-M. Berroir, N. Plaças, T. Jonckheere, et al., *Phys. Rev. B* **94**, 115311 (2016).
- <sup>10</sup> V. Freulon, A. Marguerite, J. Berroir, B. Plaças, A. Cavanna, Y. Jin, and G. Fève, *Nature Communications* **6**, 6854 (2015).
- <sup>11</sup> S. Tewari, P. Roulleau, C. Grenier, F. Portier, A. Cavanna, U. Gennser, D. Maillly, and P. Roche, *Phys. Rev. B* **93**, 035420 (2016).
- <sup>12</sup> I. Levkivskiy and E. Sukhorukov, *Phys. Rev. B* **78**, 045322 (2008).
- <sup>13</sup> A. O. Slobodeniuk, E. G. Idrisov, and E. V. Sukhorukov, *Phys. Rev. B* **93**, 035421 (2016).
- <sup>14</sup> G. Fève, A. Mahé, J. Berroir, T. Kontos, B. Plaças, D.C. Glattli, A. Cavanna, B. Etienne, and Y. Jin, *Science* **316**, 1169 (2007).
- <sup>15</sup> F. Hohls, A. C. Welker, C. Leicht, L. Fricke, B. Kaestner, P. Mirovsky, A. Müller, K. Pierz, U. Siegner, and H. W. Schumacher, *Phys. Rev. Lett.* **109**, 056802 (2012).
- <sup>16</sup> J. Waldie, P. See, V. Kashcheyevs, J. P. Griffiths, I. Farrer, G. A. C. Jones, D. A. Ritchie, T. J. B. M. Janssen, and M. Kataoka, *Phys. Rev. B* **92**, 125305 (2015).
- <sup>17</sup> J. Dubois, T. Jullien, C. Grenier, P. Degiovanni, P. Roulleau, and D. C. Glattli, *Phys. Rev. B* **88**, 085301 (2013).
- <sup>18</sup> J. D. Fletcher, P. See, H. Howe, M. Pepper, S. P. Giblin, J. P. Griffiths, G. A. C. Jones, I. Farrer, D. A. Ritchie, T. J. B. M. Janssen, et al., *Phys. Rev. Lett.* **111**, 216807 (2013).
- <sup>19</sup> S. Hermelin, S. Takada, M. Yamamoto, S. Tarucha, A. Wieck, L. Saminadayar, C. Bäerle, and T. Meunier, *Nature* **477**, 435 (2011).
- <sup>20</sup> J. Ott and M. Moskalets (2014), arXiv:1404.0185.
- <sup>21</sup> V. Kashcheyevs and P. Samuelsson, *Phys. Rev. B* **95**, 245424 (2017).
- <sup>22</sup> M. Misiorny, G. Fève, and J. Splettstoesser, *Phys. Rev. B* **97**, 075426 (2018).
- <sup>23</sup> A. Marguerite, B. Roussel, R. Bisognin, C. Cabart, M. Kumar, J. Berroir, E. Bocquillon, B. Plaças, A. Cavanna, U. Gennser, et al. (2017), submitted to PRL.
- <sup>24</sup> N. Johnson, J. D. Fletcher, D. A. Humphreys, P. See, J. P.

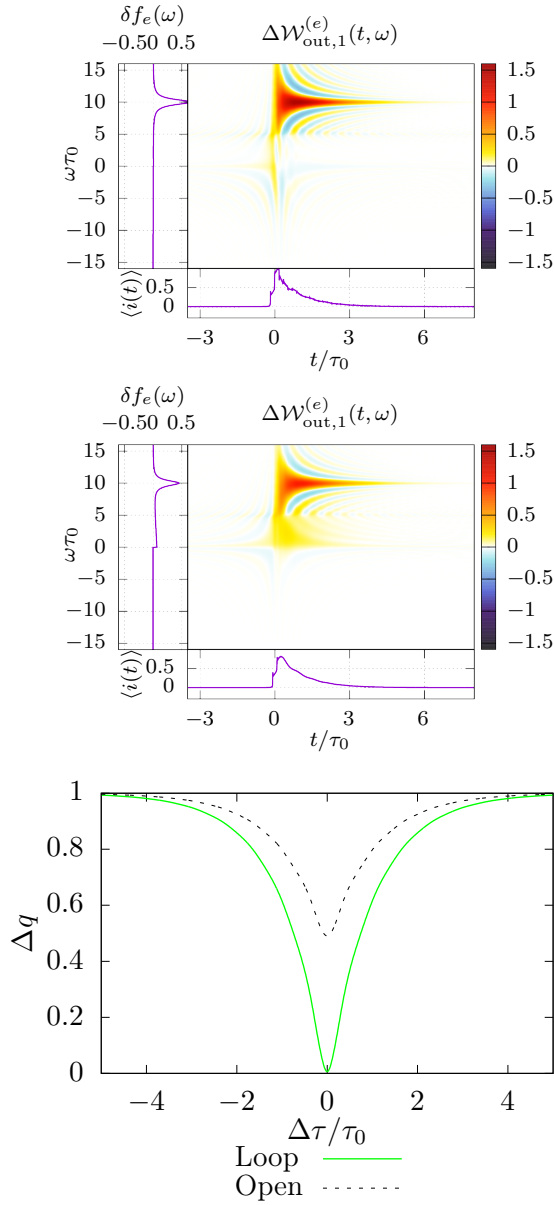


FIG. 26: (Color online) Parameters are  $w = 1 \mu\text{m}$ ,  $d = 0.4 \mu\text{m}$ ,  $\omega_0\tau_0 = 10$ . The energy of the particle is  $60 \mu\text{eV}$ , the resonance energy is at  $120 \mu\text{eV}$ .

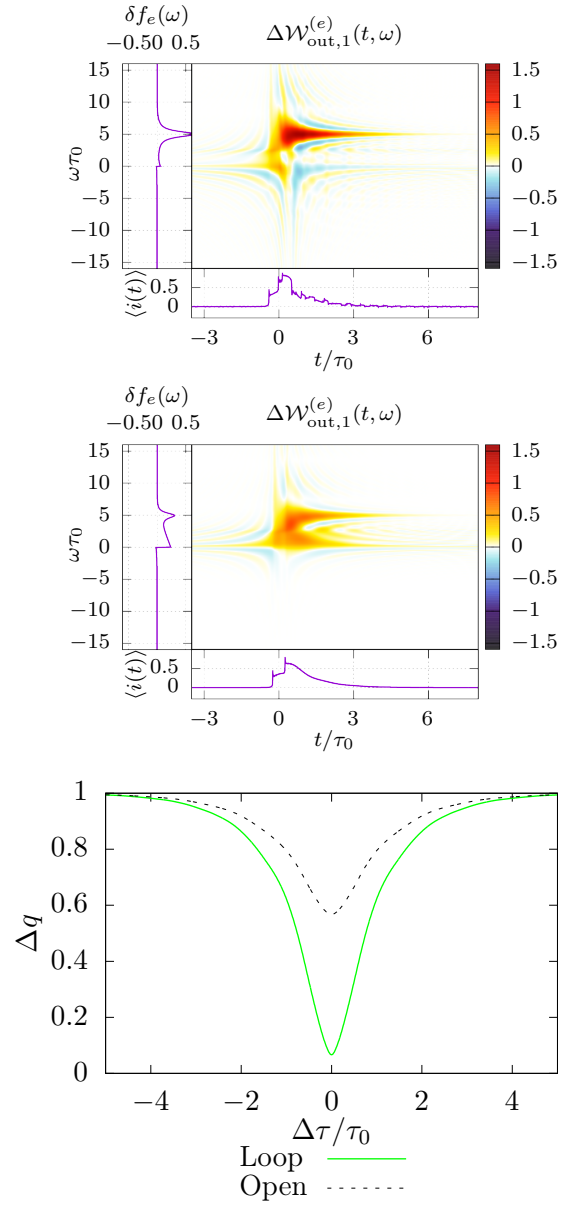


FIG. 27: (Color online) Parameters are  $w = 3 \mu\text{m}$ ,  $d = 0.5 \mu\text{m}$ ,  $\omega_0\tau_0 = 5$ . The energy of the particle is at  $30 \mu\text{eV}$ , the resonance energy at  $45 \mu\text{eV}$ . We see that sending a smaller energy excitation allows for larger loops.

Griffiths, G. A. C. Jones, I. Farrer, D. A. Ritchie, M. Pepper, T. J. B. M. Janssen, et al., Applied Physics Letters **110**, 102105 (2017).

- <sup>25</sup> P. Degiovanni, C. Grenier, and G. Fève, Phys. Rev. B **80**, 241307(R) (2009).
- <sup>26</sup> D. Ferraro, C. Wahl, J. Rech, T. Jonckheere, and T. Martin, Phys. Rev. B **89**, 075407 (2014).
- <sup>27</sup> C. Altimiras, H. Le Sueur, U. Gennser, A. Cavanna, D. Mailly, and F. Pierre, Phys. Rev. Lett. **105**, 226804 (2010).
- <sup>28</sup> P.-A. Huynh, F. Portier, H. le Sueur, G. Faini, U. Gennser, D. Mailly, F. Pierre, W. Wegschider, and P. Roche, Phys. Rev. Lett. **108**, 256802 (2012).
- <sup>29</sup> R. Glauber, Phys. Rev. **130**, 2529 (1963).

- <sup>30</sup> C. Grenier, R. Hervé, E. Bocquillon, F. Parmentier, B. Plaçais, J. Berroir, G. Fève, and P. Degiovanni, New Journal of Physics **13**, 093007 (2011).
- <sup>31</sup> G. Haack, M. Moskalets, J. Splettstoesser, and M. Büttiker, Phys. Rev. B **84**, 081303 (2011).
- <sup>32</sup> G. Haack, M. Moskalets, and M. Büttiker, Phys. Rev. B **87** (2012).
- <sup>33</sup> D. Ferraro, A. Feller, A. Ghibaudo, E. Thibierge, E. Bocquillon, G. Fève, C. Grenier, and P. Degiovanni, Phys. Rev. B **88**, 205303 (2013).
- <sup>34</sup> T. Jullien, P. Roulleau, B. Roche, A. Cavanna, Y. Jin, and D. C. Glatli, Nature **514**, 603 (2014).
- <sup>35</sup> A. Mahé, F. Parmentier, G. Fève, J. Berroir, T. Kon-

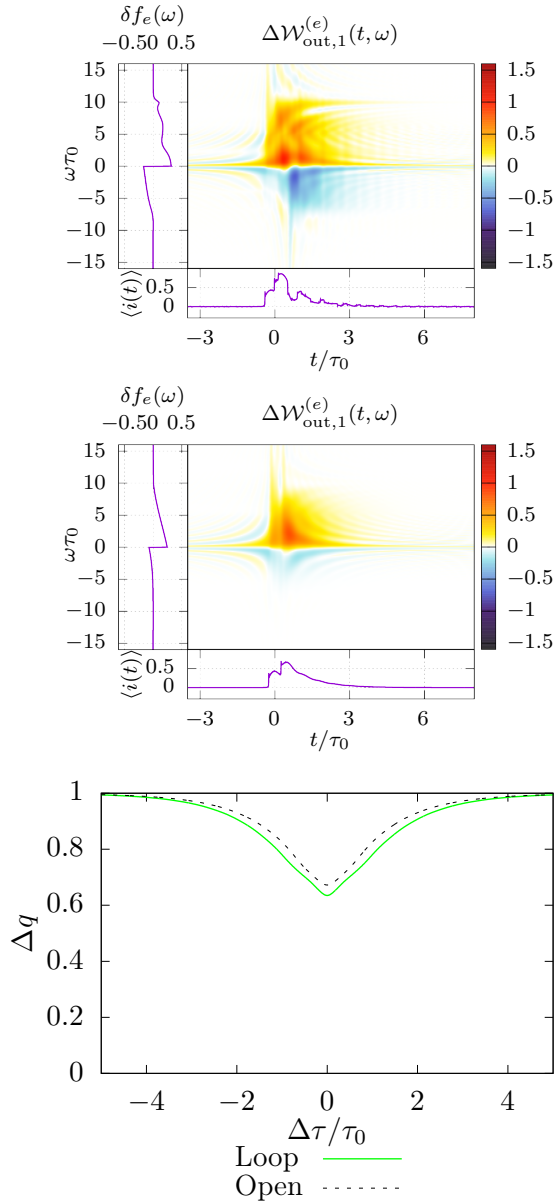


FIG. 28: (Color online) Parameters are  $w = 3 \mu\text{m}$ ,  $d = 0.5 \mu\text{m}$ ,  $\omega_0\tau_0 = 10$ . The energy of the particle is at  $60 \mu\text{eV}$ , the resonance energy at  $45 \mu\text{eV}$ . In that case, the loops does not allow protection from decoherence, and a plasmon state is emitted along with the electron.

tos, A. Cavanna, B. Etienne, Y. Jin, D. C. Glatli, and B. Plaças, *Journal of Low Temperature Physics* **153**, 339 (2008).

<sup>36</sup> A. Mahé, F. Parmentier, E. Bocquillon, J. Berroir, D. C. Glatli, T. Kontos, B. Plaças, G. Fève, A. Cavanna, and Y. Jin, *Phys. Rev. B* **82**, 201309 (2010).

<sup>37</sup> B. Roussel, C. Cabart, R. Bisognin, G. Fève, and P. Degiovanni, in preparation.

<sup>38</sup> J. Dubois, T. Jullien, F. Portier, P. Roche, A. Cavanna, Y. Jin, W. Wegscheider, P. Roulleau, and D. C. Glatli, *Nature* **502**, 659 (2013).

<sup>39</sup> L. Levitov, H. Lee, and G. Lesovik, *J. Math. Phys.* **37**,

4845 (1996).

<sup>40</sup> J. Keeling, I. Klich, and L. Levitov, *Phys. Rev. Lett.* **97**, 116403 (2006).

<sup>41</sup> C. Grenier, J. Dubois, T. Jullien, P. Roulleau, D. C. Glatli, and P. Degiovanni, *Phys. Rev. B* **88**, 085302 (2013).

<sup>42</sup> L. Landau, *Sov. Phys. JETP* **5**, 101 (1957).

<sup>43</sup> M. Devoret, D. Esteve, H. Grabert, G.-L. Ingold, H. Pothier, and C. Urbina, *Phys. Rev. Lett.* **64**, 1824 (1990).

<sup>44</sup> S. Girvin, L. Glazman, M. Jonson, D. Penn, and M. Stiles, *Phys. Rev. Lett.* **64**, 3183 (1990).

<sup>45</sup> D. Ferraro, B. Roussel, C. Cabart, E. Thibierge, G. Fève, C. Grenier, and P. Degiovanni, *Phys. Rev. Lett.* **113**, 166403 (2014).

<sup>46</sup> W. Zurek, S. Habib, and J. Paz, *Phys. Rev. Lett.* **70**, 1187 (1993).

<sup>47</sup> I. Safi and H. Schulz, *Phys. Rev. B* **52**, R1740 (1995).

<sup>48</sup> I. Safi and H. Schulz, in *Quantum Transport in Semiconductor Submicron Structures*, edited by B. Kramer (Kluwer Academic Press, Dordrecht, 1995), p. 159.

<sup>49</sup> I. Safi, *Eur. Phys. J. D* **12**, 451 (1999).

<sup>50</sup> P. Degiovanni, C. Grenier, G. Fève, C. Altimiras, H. le Sueur, and F. Pierre, *Phys. Rev. B* **81**, 121302(R) (2010).

<sup>51</sup> W. Cauer, *Archiv für Elektrotechnik* **17**, 355 (1926).

<sup>52</sup> O. Brune, *J. Math. and Phys.* **10**, 191 (1931).

<sup>53</sup> E. Bocquillon, V. Freulon, J. Berroir, P. Degiovanni, B. Plaças, A. Cavanna, Y. Jin, and G. Fève, *Nature Communications* **4**, 1839 (2013).

<sup>54</sup> I. Petković, F. I. B. Williams, and D. C. Glatli, *Journal of Physics D: Applied Physics* **47**, 094010 (2014).

<sup>55</sup> M. Hashisaka, N. Hiyama, T. Akiho, K. Muraki, and T. Fujisawa, *Nature Physics* **advance online publication**, (2017).

<sup>56</sup> H. Inoue, A. Grivnin, N. Ofek, I. Neder, M. Heiblum, V. Umansky, and D. Mahalu, *Phys. Rev. Lett.* **112**, 166801 (2014).

<sup>57</sup> A. Prêtre, H. Thomas, and M. Büttiker, *Phys. Rev. B* **54**, 8130 (1996).

<sup>58</sup> T. Christen and M. Büttiker, *Phys. Rev. B* **53**, 2064 (1996).

<sup>59</sup> G.-L. Ingold and Y. Nazarov, *Single charge tunneling* (Plenum Press, New York, 1992), vol. 294 of *NATO ASI Series B*, chap. Charge tunneling rates in ultrasmall junctions, pp. 21–107.

<sup>60</sup> E. Bocquillon, V. Freulon, J. Berroir, P. Degiovanni, B. Plaças, A. Cavanna, Y. Jin, and G. Fève, *Science* **339**, 1054 (2013).

<sup>61</sup> S. Ol'khovskaya, J. Splettstoesser, M. Moskalets, and M. Büttiker, *Phys. Rev. Lett.* **101**, 166802 (2008).

<sup>62</sup> V. Volkov and S. Mikhailov, *Sov. Phys. JETP* **67**, 1639 (1988).

<sup>63</sup> N. Kumada, H. Kamata, and T. Fujisawa, *Phys. Rev. B* **84**, 045314 (2011).

<sup>64</sup> N. Kumada, P. Roulleau, B. Roche, M. Hashisaka, H. Hibino, I. Petković, and D. C. Glatli, *Phys. Rev. Lett.* **113**, 266601 (2014).

<sup>65</sup> D. S. Wei, T. van der Sar, J. D. Sanchez-Yamagishi, K. Watanabe, T. Taniguchi, P. Jarillo-Herrero, B. I. Halperin, and A. Yacoby, *Science Advances* **3**, e1700600 (2017).

<sup>66</sup> C. Wahl, J. Rech, T. Jonckheere, and T. Martin, *Phys. Rev. Lett.* **112**, 046802 (2014).

<sup>67</sup> E. Berg, Y. Oreg, E.-A. Kim, and F. von Oppen, *Phys. Rev. Lett.* **102**, 236402 (2009).

- <sup>68</sup> H. Kamata, N. Kumada, M. Hashisaka, K. Muraki, and T. Fujisawa, *Nature Nanotechnology* **9**, 177 (2014).
- <sup>69</sup> V. I. Talyanskii, J. M. Shilton, M. Pepper, C. G. Smith, C. J. B. Ford, E. H. Linfield, D. A. Ritchie, and G. A. C. Jones, *Phys. Rev. B* **56**, 15180 (1997).
- <sup>70</sup> H. Kamata, T. Ota, K. Muraki, and T. Fujisawa, *Phys. Rev. B* **81**, 085329 (2010).
- <sup>71</sup> I. Petković, F. I. B. Williams, K. Bennaceur, F. Portier, P. Roche, and D. C. Glattli, *Phys. Rev. Lett.* **110**, 016801 (2013).
- <sup>72</sup> R. Forster, *Bell System Tech. J.* **3**, 259 (1924).
- <sup>73</sup> C. Neuenhahn and F. Marquardt, *New Journal of Physics* **10**, 115018 (2008).
- <sup>74</sup> C. Neuenhahn and F. Marquardt, *Phys. Rev. Lett.* **102**, 046806 (2009).
- <sup>75</sup> These figures correspond to the ideal  $\nu = 1$  case which is not the case that has been experimentally studied. In the experiments, extrinsic decoherence induced by the second edge channel leads to much shorter coherent propagation distance for such energy resolved excitations.
- <sup>76</sup> In this equation, we adopt the convention that  $\binom{n}{k} = 0$  if  $k > n$  or  $k < 0$ .